INVESTIGATION OF MAGNETIC ANISOTROPIES AND MAGNETIZATION DYNAMICS IN SOFT MAGNETIC MATERIALS

by

ABHISHEK SRIVASTAVA

TIM MEWES, COMMITTEE CHAIR
CLAUDIA MEWES
ARUNAVA GUPTA
GARY MANKEY
CONOR HENDERSON

A DISSERTATION

Submitted in partial fulfillment of the requirements
for the degree of Doctor of Philosophy
in the Department of Physics and Astronomy
in the Graduate School of
The University of Alabama

TUSCALOOSA, ALABAMA

2020

Copyright 2020 by Abhishek Srivastava
ALL RIGHTS RESERVED

ABSTRACT

Magnetic anisotropy and damping are two main properties that determine the characteristics of many magnetic devices such as inductors, transformers, hard drives, GMR sensors, MRAM etc. The magnetic materials used in these devices can be in different forms. For example spintronic devices are made of thin films (single crystalline or polycrystalline), and thus in these systems the effect of the substrate such as lattice mismatch, strain etc plays an important role in determining and manipulating magnetic properties. In case of transformers and inductors magnetic materials are made of bulk ferrite or as thin ($\sim 20\ \mu m$) ribbons of nanocomposite alloys. This dissertation gives a basic introduction of the magnetization dynamics and the physics and instrumentation of FMR. The induced anisotropy and magnetization dynamics of $Co_{74.6}Fe_{2.7}$-$Mn_{2.7}Nb_4Si_2B_{14}$ (at %) melt-spun, soft magnetic alloy ribbons after various secondary processing treatments was studied by broadband ferromagnetic resonance (FMR) technique. A new method of determining the relative permeability of these ribbons is discussed and compared to the established vibrating sample magnetometry (VSM) and the toroid method. This new method of determining the permeability does not require information about the volume or mass of the sample nor does it require any special sample preparation procedure.

Another study presented in this thesis investigates the temperature dependence of the magnetic anisotropy of a single crystal magnetite (Fe_3O_4) thin film grown on $MgGa_2O_4$ substrate. The aim of this study is to characterize the magnetization dynamics and magnetic anisotropy of this magnetite thin film through the Verwey transition. The broadband ferromagnetic resonance

study of this film suggest a continous structural transition from cubic to monoclinic phase as the temperature is decreased.

Finally the magnetic properties of polycrystalline semiconducting spinel $CdCr_2S_4$ films grown by low-pressure metal organic chemical vapor deposition are studied. This includes the investigation of the paramagnetic to ferromagnetic phase transition using broadband FMR. The effective magnetization vs temperature data shows a relatively sharp transition compared to magnetization vs temperature data obtained from VSM. The study shows that these differences can be traced to the different roles the applied magnetic field has when analyzing the data from these two techniques.

DEDICATION

To

My wife, Ashima and my family members

LIST OF ABBREVIATIONS AND SYMBOLS

α	Gilbert damping constant
α_{eff}	Effective Gilbert damping constant
ΔH_{PP}	Peak to peak lineewidth
$\gamma\prime$	Gyromagnetic ratio
μ_0	Vacuum permeability
ω	Angular frequency
θ	Polar angle
ϕ	Azimuthal angle
AFM	Atomic force microscope/microscopy
DC	Direct current
GMR	Giant magnetoresistance
H_{eff}	Effective field
H_k	Anisotropy field
h_{mw}	Microwave field
H_{res}	Resonance field
FMR	Ferromagnetic resonance
f	FMR frequency
LLG	Landau-Lifshitz-Gilbert
M	Magnetization

M_s	Saturation magnetization
M_{eff}	Effective magnetization
PPMS	Physical property measurement system
RAM	Random access memory
STT	Spin transfer torque
VSM	Vibrating sample magnetometer
XRD	X-ray diffraction

ACKNOWLEDGMENTS

First and foremost, I would like to express my deepest gratitude to my advisor Prof. Tim Mewes for being a great advisor and a friend. This dissertation would not have been possible without his support and guidance. I am also thankful to him for his suggestions given to me time to time, which not only helped me in my research but also played crucial role in overcoming my personal difficulties. I also acknowledge the financial support from the NASA Grant NASA CAN80NSSC18M0023 and the Department of Physics and Astronomy.

Next, I would like to thank my committee members, Prof. Arunava Gupta, Prof. Claudia Mewes, Prof. Gary J. Mankey, and Prof. Conor Henderson for their inputs during my PhD. I Also appreciate the help and support from my friends, colleagues and collaborators Dr. Behrouz Khodadadi, Dr. Jamileh Beik Mohammadi, Dr. Amit Singh, Dr. Chao Pang, Dr. Zhong Li, Sudhir, Anish, Arjun, Ashok, Bhuwan, Kayla, Alicia, and Dr. Thomas Burton. I especially thank to Dr. Alex M. Leary (NASA), Dr. Ronald D. Noebe (NASA) for providing samples and for useful discussions, I also thank Prof. Gregory B. Thompson (University of Alabama) for allowing me to work in his laboratory.

My special thanks for technical support from department of Physics machine shop staff and electronics technicians David Key, Joe Howell, Michael Perrigin, Danny whitcomb and Jason Kuykendall. I am also thankful to the staff at MINT center - Jon steen, Casey McDow, Jamie Crawford, Carrie Martin and Dr. Michael Buettner. And finally, I thank Nancy and Karen, the admisnistrative staff from the department of Physics.

CONTENTS

ABSTRACT ii

DEDICATION iv

LIST OF ABBREVIATIONS AND SYMBOLS v

ACKNOWLEDGMENTS vii

LIST OF TABLES xii

LIST OF FIGURES xiii

CHAPTER 1 INTRODUCTION 1

1.1 Magnetic anisotropy 1

1.2 Magnetization dynamics 2

1.3 Magnetization damping 4

1.4 Ferromagnetic resonance 6

1.5 Experimental setup 7

1.6 Magnetic anisotropy and damping in soft magnetic materials 10

CHAPTER 2 BROADBAND CHARACTERIZATION OF STRESS INDUCED ANISOTROPY IN NANOCOMPOSITE $Co_{74.6}Fe_{2.7}Mn_{2.7}Nb_4Si_2B_{14}$ 13

2.1 Abstract 13

2.2 Introduction 14

2.3 Experimental techniques 15

2.4 Results 16

2.5 Discussion 26

2.6 Conclusion 28
2.7 Acknowledgement 29
2.8 References 30
CHAPTER 3 FERROMAGNETIC RESONANCE STUDY OF THE VERWEY PHASE TRANSITION OF MAGNETITE THIN FILM ON $MgGa_2O_4$ (001) 33
3.1 Abstract 33
3.2 Introduction 34
3.3 Experimental details 35
3.4 Interpretation of FMR data 35
3.5 Results 38
3.6 Conclusion 43
3.7 Acknowledgements 43
3.8 Appendix 44
3.9 References 46
CHAPTER 4 MAGNETIC PROPERTIES OF SEMICONDUCTING SPINEL $CdCr_2S_4$ FILMS GROWN BY LOW-PRESSURE METAL ORGANIC CHEMICAL VAPOR DEPOSITION 48
4.1 Abstract 48
4.2 Introduction 49
4.3 Experimental section 51
4.4 Results and discussion 54
4.5 Conclusion 63
4.6 Acknowledgment 63
4.7 Appendix 64
4.8 References 66
CHAPTER 5 CONCLUSION 70

REFERENCES 73

LIST OF TABLES

2.1 Parameters extracted from Kittel plot 18

2.2 Parameters extracted from linewidth vs frequency data 22

2.3 Permeability obtained using the toroid method, vibrating sample magnetometry (VSM), and ferromagnetic resonance (FMR). In the case of the FMR results, the effective magnetization of the respective sample obtained using broadband FMR was used to calculate the value listed in the table. 25

4.1 Values of effective magnetization $M_{eff,0}$ and gyromagnetic ratio γ' obtained from broadband FMR measurements. 61

LIST OF FIGURES

1.1 Precession of magnetization in effective magnetic field. 3

1.2 Schematic of the coordinate system used for equation 1.5 4

1.3 A typical field swept FMR spectrum measured at a fixed frequency (10 GHz). . . . 7

1.4 Block diagram of FMR detection scheme. 8

1.5 Sketch of an FMR spectrometer. 8

1.6 A photo of room temperature FMR setup. 9

2.1 Coordinate system describing the applied DC field for in-plane disc measurements. 17

2.2 a) Field swept FMR spectrum measured at 46 GHz for a sample stress annealed at 100 MPa. b) Frequency dependence of FMR resonance field of all the samples. The continuous lines represent the fit to the experimental data using equation 2.1. . 18

2.3 (a) Effective magnetization, M_{eff}, and (b) the reduced gyromagnetic ratio, γ', extracted from broadband FMR measurements for all the samples. The data points represent the different stress annealed conditions, the dashed horizontal line represents the corresponding parameters of the as-cast ribbon, and dotted line corresponds to the ribbon sample annealed in a transverse magnetic field (TMF). . . 19

2.4 In-plane angular variation of resonance field at 20 GHz of a) as-cast, b) annealed in transverse magnetic field (TMF), c) stress annealed at 50 MPa, d) 100 MPa, e) 150 MPa and f) 200 MPa. Zero degree corresponds to the spin-casting direction and also the stress axis in SA samples. The experimental data is shown as blue squares, and the fit is shown as a continuous line. 21

2.5 Frequency dependence of the FMR linewidth of all $Co_{74.6}Fe_{2.7}Mn_{2.7}Nb_4Si_2B_{14}$ samples. The continuous line is fit to the data using equation 2.5 22

2.6 (a) Linewidth extrapolated to zero field and (b) effective damping constant extracted from the frequency dependence of linewidth, obtained from broadband FMR measurements for the as-cast $Co_{74.6}Fe_{2.7}Mn_{2.7}Nb_4Si_2B_{14}$ alloy and after different annealing treatments. The data points represent the different stress annealed conditions, the dashed horizontal line represents the corresponding parameters of the as-cast ribbon, and dotted line corresponds to the ribbon sample annealed in a transverse magnetic field (TMF). 23

2.7 Hysteresis curves from a) 100 MPa SA sample and b) TMF sample measured with the field applied along the easy ($\theta = \frac{\pi}{2}$) and hard directions ($\theta = 0$). Radial susceptibility χ plots for c) SA and d) TMF samples, which show the symmetry of the induced anisotropy and saturating fields. 26

2.8 Angle dependent susceptibility χ, measured using VSM at H = 100 A/m for $Co_{74.6}Fe_{2.7}Mn_{2.7}Nb_4Si_2B_{14}$ TMF and 100 MPa SA samples. Fits correspond to $\chi_{hard} + \Delta\chi \cdot \sin^2\theta$. 27

2.9 Dependence of the uniaxial anisotropy field, H_u, on the stress during annealing. Data obtained from broadband FMR measurements are shown as black symbols whereas the more precise data obtained from in-plane angle dependent measurements are shown in blue. 28

2.10 Comparison of the relative permeability as a function of the stress during annealing determined using the toroid method, VSM, and using the anisotropy field (H_u) obtained from FMR, assuming $M_s = M_{eff}$. 28

3.1 Coordinate system for the sample with respect to cube axis. [001] is normal to the film plane. [010] is the monoclinic *c* axis and *a* and *b* are the axes of monoclinic phase, in the plane containing [001] and [100] direction. 36

3.2 Frequency dependence of FMR resonance field along the [010] direction (blue symbols, in-plane hard axis) and [110] direction (red symbols, in-plane easy axis) at 300 K for a 30 nm thick Fe_3O_4 film grown on $MgGa_2O_4$ (001). Solid lines are a fit to the Kittel equations (1) and (2) with shared fitting parameters. 37

3.3 Resonance field vs Temperature at 30 GHz for external magnetic field applied along [010] direction (blue symbols) and [110] direction (red symbols). Solid lines are guide to the eye. 39

3.4 Temperature dependence of parameters extracted from Kittel fit, (a) effective magnetization, (b) reduced gyromagnetic ratio γ', and (c) cubic magnetocrystalline anisotropy. 41

3.5 The temperature dependence of the in-plane uniaxial anisotropy below 120 K. . . . 42

3.6 The temperature dependence of linewidth at f=30 GHz when the applied field is parallel to (a) [010] and (b) [110] direction. 42

3.7 (a) Linewidth dependence on the frequency for the external field in cubic [010] direction at different temperatures. Solid line is the fit to the equation 3.5. (b) The effective damping vs. temperature. 43

3.8 FMR spectra at different temperatures at 30 GHz, for the external field along [010] direction. The spectra at 75 K is amplified 10 times for comparison. 45

4.1 Growth of nanostructured $CdCr_2S_4$ film and its crystal structure and morphology characterization. (a) Schematic diagram of the home-built low-pressure MOCVD setup. (b) XRD pattern of polycrystalline $CdCr_2S_4$ film deposited on borosilicate glass substrate. The inset displays the crystal structure of spinel $CdCr_2S_4$ (Cd, pink; Cr, blue; S, yellow). (c) Low- and (d) high-magnification planar SEM images. (e) High-magnification cross-sectional SEM images. (f) 2D AFM image of the $CdCr_2S_4$ film. measurements. 54

4.2 Composition and chemical states characterization of the nanostructured $CdCr_2S_4$ film. (a) FESEM image; mixed and individual elemental mapping of the deposited film. (b) EDS spectrum and elemental composition of the film. (c) XPS survey spectrum; high-resolution XPS spectra of Cd 3d, Cr 2p, and S 2p of the $CdCr_2S_4$ film. 55

4.3 Optical properties characterization of the $CdCr_2S_4$ film (thickness of 580 nm). (a) UV-vis absorption spectrum of the $CdCr_2S_4$ film grown on borosilicate glass substrate. The inset shows a photograph of the film. (b) Tauc plot of $(\alpha h\nu)^2$ vs $h\nu$ to determine the band gap of the films. The inset shows the band gap vs lower end of photon energy for fitting. 57

4.4 Magnetic characterization of the $CdCr_2S_4$ film (thickness of 580 nm). (a) Magnetization (M) versus temperature (T) of the film measured at different magnetic fields. The inset shows plots of the slope, dM/dT, calculated from (a). (b) Representative isothermal M-H measurements and (c) Arrott plots from 58 to 109 K with temperature steps of 3 K. (d) Magnetization as a function of field measured at 5 and 300 K. The inset displays an enlarged portion of the hysteresis loop measured at 5 K. 58

4.5 CW EPR characterization of the nanostructured $CdCr_2S_4$ film (thickness of 580 nm). (a) EPR spectra as a function of temperature for the film aligned parallel to the external applied magnetic field and (b) perpendicular to the external magnetic field. (c) Line width as a function of temperature for both magnetic field orientations. (d) Resonance field as a function of temperature for both magnetic field orientations. (e) Resonance field as a function of direction of external field (0° perpendicular to film plane and 90° parallel to film plane) at different temperatures. (f) Inverse double integral of CW EPR spectra characterizing the spin susceptibility of the $CdCr_2S_4$ film. The inset displays an enlarged portion around the Curie temperature T_C 59

4.6 Broadband FMR characterization of the $CdCr_2S_4$ film. (a) Representative resonance field as a function of microwave frequency at 70 K for both magnetic field orientations. The continuous line is fit to Kittel's equation. A typical spectrum is shown in the inset. (b) Linewidth as a function of frequency at different temperatures for external magnetic field parallel to film plane and (c) perpendicular to film plane. (d) Kittel plots at different temperatures for external magnetic field parallel to film plane and (e) perpendicular to film. (f) Plot of the extracted g factor as a function of temperature. 61

4.7 The reactions for formation and crystal structure of $Cr(S_2CNEt_2)_3$ and dimerized $Cd(S_2CNEt_2)_2$. 64

4.8 Thermogravimetric analysis (TGA) curves for the decomposition of (a) $Cd(S_2CNEt_2)_2$ and (b) $Cr(S_2CNEt_2)_3$. 65

CHAPTER 1

INTRODUCTION

1.1 Magnetic anisotropy

Magnetic anisotropy of a magnetic material is observed if the internal energy (magnetic anisotropy energy) depends on the direction of the magnetization. If the anisotropy originates from the crystal structure of the material it is called magnetocrystalline anisotropy, which is caused by the interaction of the orbital motion of the electron (which is linked to the crystal structure of the material) with the spin of the electron, i.e. the spin-orbit interaction. Magnetocrystalline anisotropy is commensurate with the crystal structure. Due to magnetic anisotropy there are the directions along which it is easy to magnetize the magnetic material (easy axes) and along certain direction it is hard to magnetize (hard axes). This anisotropy is described phenomenologically in terms of a series expansion of direction cosines of magnetization relative to the crystal axes. For example in a cubic crystal anisotropy contribution to the magnetic free energy density can be written as

$$E_{aniso} = K_0 + K_1(\alpha_1^2\alpha_2^2 + \alpha_2^2\alpha_3^2 + \alpha_3^2\alpha_1^2) + K_2(\alpha_1^2\alpha_2^2\alpha_3^2) + ... \tag{1.1}$$

where $\alpha_1, \alpha_2, \alpha_3$ are the direction cosines and K_1, K_2 are the constants for a particular material and are called anisotropy constants expressed in erg/cm^3 (cgs) or J/m^3 (SI). The anisotropy constants can be temperature dependent. Generally higher powers are neglected in the expansion and sometimes K_2 is small and can be neglected. In the absence of an external field the anisotropy favors the spontaneous magnetization along the easy axis. For a small deviation of the magnetization away from the easy axis the anisotropy acts like a magnetic field parallel to the direc-

tion of easy axis trying to bring the magnetization back, parallel to the easy axis. This internal field is called the anisotropy field denoted by symbol H_k. Besides magnetocrystalline anisotropy, there may be other sources of anisotropy in a magnetic system. For example shape anisotropy originating from dipole-dipole interaction and the shape of the material; induced anisotropy produced by treatment of magnetic materials for example rolling, stress annealing and photo-induced anisotropy [1, 2]; interface anisotropy due to reduced symmetry at the interface. In this dissertation magnetocrystalline anisotropy of magnetite thin film and induced anisotropy in amorphous magnetic alloy are investigated in detail.

1.2 Magnetization dynamics

Magnetization dynamics in a ferromagnet deals with the time evolution of the magnetization when it is disturbed from its equilibrium orientation. In absence of any external perturbation the magnetic moments will subsequently orient in the direction of total effective field, H_{eff}. If a magnetic moment is perturbed from its equilibrium orientation, the moment will precess about the effective magnetic field before this precession dies out due to energy dissipation.

In a ferromagnet the magnetization dynamics is described by the Landau-Lifshitz-Gilbert (LLG) [3, 4] equation 1.2.

$$\frac{\partial \vec{M}}{\partial t} = -\gamma(\vec{M} \times \vec{H}_{eff}) + \frac{\alpha}{M} \cdot \vec{M} \times \frac{\partial \vec{M}}{\partial t} \tag{1.2}$$

where $\vec{M}$ is the magnetization, γ is the gyromagnetic ratio, $\vec{H}_{eff}$ is the effective magnetic field, and α is the dimensionless Gilbert damping parameter. Equation 1.2 describes the rate of change of the magnetization, which has two components. The first component is the precession term which describes the precession of magnetization around the effective field and the second term is the damping term that describes the relaxation towards the effective field. Figure 1.1 is a sketch depicting the motion of the magnetization after it is perturbed by a microwave field.

The LLG equation can be solved by linearizing the equation and finding the dispersion re-

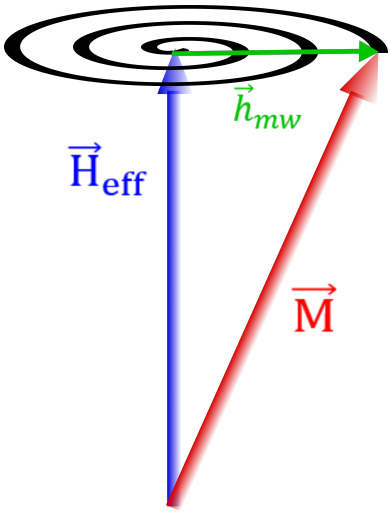

Figure 1.1: Precession of magnetization in effective magnetic field.

lation [5, 6]. For an external field applied in the plane of the film, the dispersion relation can be written as in equation 1.3

$$f = \gamma' \sqrt{(H_{res} + H_k)(H_{res} + 4\pi M_{eff} + H_k)} \tag{1.3}$$

Where f is the frequency of precession, H_{res} is the resonance field, γ' is $\gamma/2\pi$, H_K is the in-plane anisotropy field, and M_{eff} is the effective magnetization as defined in equation 1.4. The equation 1.3 is the simplest form of a dispersion relation in a thin film. If there are contributions from other forms of anisotropy for example induced anisotropy, exchange bias or magnetocrystalline anisotropy the dispersion relation becomes more complicated [7, 8].

The effective magnetization is given by :

$$4\pi M_{eff} = 4\pi M_s - \frac{2K_u}{M_s} \tag{1.4}$$

where M_s is the saturation magnetization and K_u is the perpendicular anisotropy constant. The effective magnetization in the dispersion relation appears due to the presence of the demagnetizing field ($4\pi M_s$) and the uniaxial perpendicular anisotropy field ($H_u = \frac{2K_u}{M_s}$). Both anisotropy fields are perpendicular to the film plane and both have the same angular dependence and there-

fore most of the time it is not possible to separate the contributions from these two terms.

Another approach of deriving the dispersion relation is writing the energy functional of the system, then minimizing the energy with respect to the parameters to find the equillibrium condition of the magnetization. And then the Smit-Beljers formula [9] given by equation 1.5 can be used to derive the dispersion relation.

$$\left(\frac{\omega}{\gamma}\right) = \frac{1}{M_s \sin\theta}\left[\frac{\partial^2 E}{\partial\theta^2}\frac{\partial^2 E}{\partial\phi^2} - \left(\frac{\partial^2 E}{\partial\theta\partial\phi}\right)^2\right]^{\frac{1}{2}} \tag{1.5}$$

Where ω is the angular frequency, γ is the gyromagnetic ratio, θ and ϕ are the polar and azimuthal angle of the magnetization $\vec{M}$, and M_s is the saturation magnetization, E is the magnetic free energy of the system. The above equation is evaluated at the equilibrium angles θ_0 and ϕ_0 as defined in figure 1.2 .

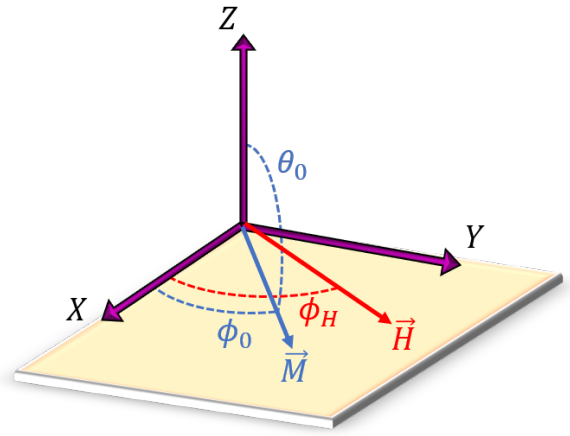

Figure 1.2: Schematic of the coordinate system used for equation 1.5

1.3 Magnetization damping

As mentioned in the previous section, once the magnetization is perturbed, it will relax back to its equillibrium orientation by dissipating the energy to the lattice system. The second term in the LLG equation 1.2 is the damping term describing this relaxation. It is a phenomenological term because the physical origin of the damping is still not clear and is an active area of research.

However, this phenomenological term is very successful in describing the spin dynamics and a number of mechanisms have been identified that lead to this form of a dissipative term. The energy from the FMR mode is finally transferred to the lattice system but this energy transfer could be direct or via intermediate states for example degenerate spin waves by two-magnon scattering [10]. Depending on the magnetic system there can be other sources of energy dissipation for example in a metallic ferromagnet eddy current is induced due to time varying magnetic field [11, 12]. Furthermore in case of ferromagnet/metal interfaces the precessing magnetization in the ferromagnet induces a spin current which can flow into the metal, this also contributes to the dissipation and is known as spin-pumping[13].

The FMR linewidth, ΔH_{PP} defined in the next section characterizes the damping in the magnetic system. Magnetic inhomogeneities in the sample also contribute to the linewidth but they are independent of frequency. The relation between ΔH_{PP} and damping is given by the equation 1.6 [14]

$$\Delta H_{PP} = \frac{1}{\sqrt{3}} \frac{\alpha}{|df/dH|} \frac{\gamma'}{M_s} \left[\frac{\partial^2 E}{\partial \theta^2} + \frac{1}{\sin^2 \theta} \frac{\partial^2 E}{\partial \phi^2} \right] \approx \frac{2}{\sqrt{3}} \frac{\alpha}{\gamma'} \frac{f}{\cos \beta} \tag{1.6}$$

Where α is the Gilbert damping constant, E is the magnetic free energy, γ' is reduced gyromagnetic ratio ($\gamma/2\pi$) and β is the angle between the magnetization and the external magnetic field. For a large enough external field applied along the easy or hard direction, the magnetization will be parallel to the external field which leads to $\beta = 0$. To include the effect of magnetic inhomogeneity, a constant term ΔH_0 is added to the equation 1.6 and thus the final expression which is generally used for linewidth analysis is equation 1.7

$$\Delta H_{PP} = \Delta H_0 + \frac{2}{\sqrt{3}} \frac{\alpha}{\gamma'} f \tag{1.7}$$

In a broadband FMR measurement where ΔH_{PP} is determind at several frequencies, fitting ΔH_{PP} vs f data using equation 1.7 the damping constant α and inhomogeneous linewidth ΔH_0.

1.4 Ferromagnetic resonance

Ferromagnetic resonance (FMR) is a very powerful and sensitive technique for studying magnetic properties of ferromagnetic thin films for example magnetic anisotropy, gyromagnetic ratio, magnetization and relaxation mechanism. FMR was first observed by Griffiths [15] and the theory of FMR was first given by Kittel [16]. FMR analysis requires the sample to be saturated, thus all the moments are considered to be parallel to each other and no domains exist in the sample. A small alternating field transverse to the effective field H_{eff} leads to the precession of the moment around H_{eff}. The frequency of this precession is in the gigahertz range for ferromagnetic materials, i.e. within the microwave range of the electromagnetic spectrum. Physically FMR is the uniform mode (wave vector $\vec{k} = 0$) excitation of the spin system which means all the magnetic moments precess with the same phase, this is the lowest energy excitation of the spin system. There can be higher modes of excitation, i.e. spin waves with non-zero wavevector which can be excited due to defects in the system or due to the geometry of the system.

In a typical FMR measurement, a quasi-static magnetic field $\vec{H}$ is applied to the sample under investigation. A microwave field $\vec{h}_{mw}$ oscillating at a frequency in the GHz range is applied perpendicular to the quasi-static field. At a fixed microwave frequency the quasi-static field is swept. At the resonance field there is an increased absorption of microwave power in the sample and thus, the transmitted power through the sample is reduced. This transmitted power is detected by a diode using a lock-in technique. The absorption profile is typically Lorentzian in shape and the system records the first derivative of the absorption profile as shown in figure 1.3.

The FMR spectra is fitted by the following expression [17, 18].

$$y = \frac{a\left(\frac{H_{res}-H}{\Delta H_{PP}}\right) + 9b - 3b\left(\frac{H_{res}-H}{\Delta H_{PP}}\right)^2}{\left[3 + \left(\frac{H_{res}-H}{\Delta H_{PP}}\right)^2\right]^2} \tag{1.8}$$

Where y is the FMR signal, H is the applied magnetic field, H_{res} is the resonance field, ΔH_{PP} is the peak to peak linewidth and a and b are the amplitudes of absorption and dispersion part of the

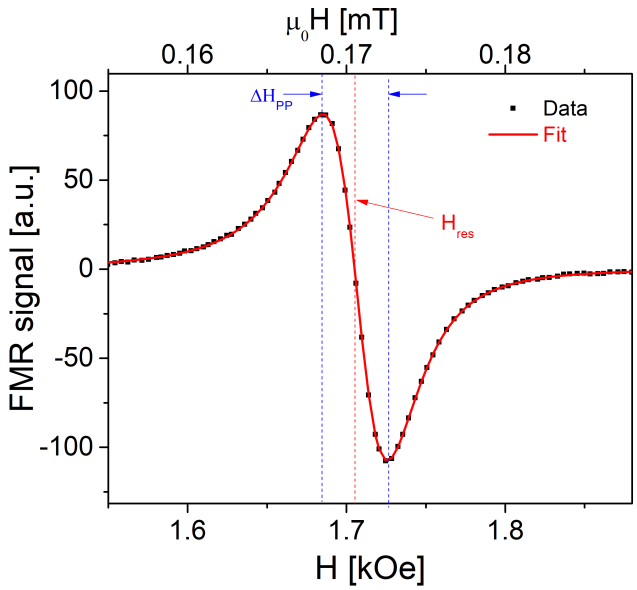

Figure 1.3: A typical field swept FMR spectrum measured at a fixed frequency (10 GHz).

signal.

1.5 Experimental setup

The experimental approach for detection of ferromagnetic resonance is similar to absorption spectroscopy as depicted by a simple block diagram in figure 1.4. A microwave source transmits the microwave of a fixed frequency and fixed power to the sample through a waveguide, and the power transmitted through the sample is detected by a Schottky diode which outputs a DC voltage proportional to the microwave power it receives. Figure 1.5 shows a sketch of an FMR spectrometer. The external field produced by an electromagnet is modulated by a pair of modulation coils.

To increase the sensitivity of detection, a lock-in technique using is used [19, 20]. In our experimental setup the external static magnetic field H_0 is modulated by a sinusoidal field at a frequency of 800 Hz with field amplitude H_m, where $H_m \ll H_0$ (equation 1.9).

$$H(t) = H_0 + H_m \cos \omega_m t \tag{1.9}$$

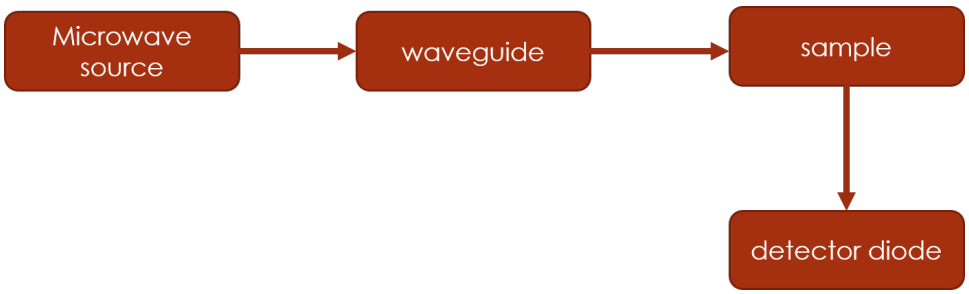

Figure 1.4: Block diagram of FMR detection scheme.

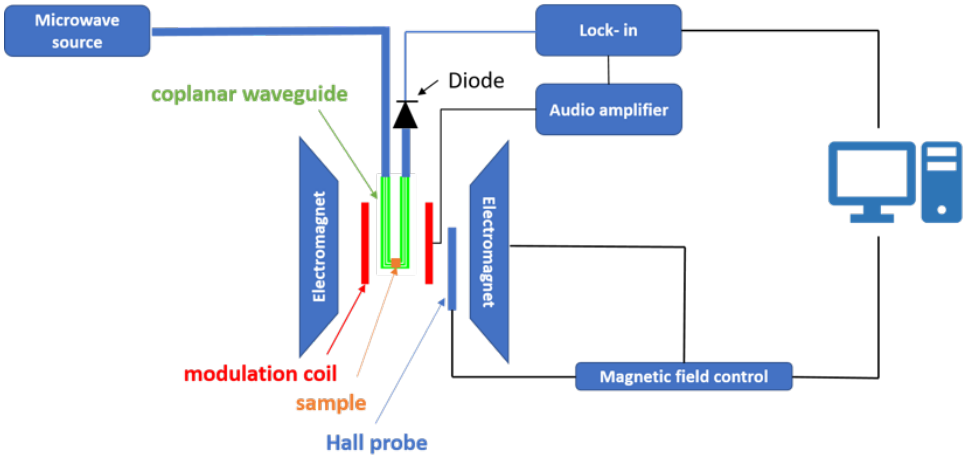

Figure 1.5: Sketch of an FMR spectrometer.

A modulated magnetic field leads to a modulation of the transmitted power through the sample, which leads to a detector voltage modulated at the same frequency as the magnetic field modulation frequency. But the noise in the system, being a random process is not affected (equation 1.10).

$$\begin{aligned} V_{FMR}(H) &= V_{FMR}(H_0 + H_m \cos \omega_m t) + V_{noise} \\ &\approx V_{FMR}(H_0) + \left.\frac{\partial V_{FMR}}{\partial H}\right|_{H=H_0} \cdot H_m \cos \omega_m t + \ldots + V_{noise} \end{aligned} \tag{1.10}$$

Here V_{FMR} is expanded using Taylor's approximation and V_{noise} is the noise. Inside the lock-in detector this voltage is multiplied by a reference voltage V_{ref} (equation 1.11) with same frequency as the modulation field. This results in a constant term (second term in the equation 1.12) along with other time dependent terms with frequency ω_m and $2\omega_m$. Within the lock-in amplifier

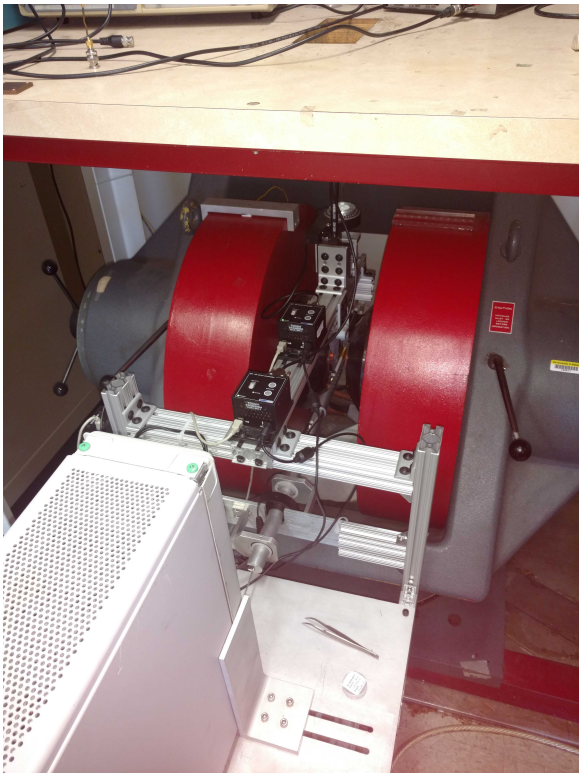

Figure 1.6: A photo of room temperature FMR setup.

this signal is fed to a low pass filter so that only the constant term remains and the other terms including the noise terms are eliminated.

$$V_{ref}(t) = V_0 \cos(\omega_m t + \phi) \tag{1.11}$$

$$\begin{aligned} V_{FMR} \cdot V_{ref} = V_{FMR} H_0 \cdot V_0 \cos(\omega_m t + \phi) + \frac{V_0}{2} \frac{\partial V_{FMR}}{\partial H}\bigg|_{H=H_0} \cdot H_m \cos\phi + \\ \frac{V_0}{2} \frac{\partial V_{FMR}}{\partial H}\bigg|_{H=H_0} \cdot H_m \cos(2\omega_m t + \phi) + ... + V_{noise} \cdot V_0 \cos(\omega_m t + \phi) \end{aligned} \tag{1.12}$$

So the strength of the signal is proportional to the reference voltage V_0, amplitude of the modulation field H_m and the derivative of the diode voltage with respect to the applied field $\frac{\partial V_{FMR}}{\partial H}$, this is the reason why when using a lock-in technique the output signal is proportional to the first derivative of the absorption.

1.6 Magnetic anisotropy and damping in soft magnetic materials

The study of the origin of magnetic anisotropy and damping in magnetic materials is of great importance and investigation of these properties in soft magnetic materials are specifically interesting due to their use in many devices. Emerging magnetic memories like STT-RAM require materials with a low damping coefficient [21], magnetic media require perpendicular magnetic anisotropy (PMA) [22] and materials for transformer applications are desired to have tunable anisotropy in order to adjust their permeability [23]. Therefore understanding these properties will help in designing materials with desired anisotropy and damping. In this work the ferromagnetic resonance technique is used to study magnetic anisotropy and magnetic damping in soft ferromagnets.

As discussed in section 1.1, magnetic anisotropy can have different origins. In nanocomposite magnetic alloys the magnetic anisotropy is induced in the alloy by applying stress during annealing. The anisotropy induced in this alloy is uniaxial and depends on the magnitude of stress applied during annealing. This property enables designing a material with tunable permeability which makes this alloy a very good candidate for core materials for transformer applications. In Chapter 2 the magnetic anisotropy and damping in nanocomposite $Co_{74.6}Fe_{2.7}Mn_{2.7}Nb_4Si_2B_{14}$ alloy is studied and a method for determining the permeability using results from FMR was discovered. The finding is important because controlling the properties at industrial scale requires regular monitoring and the method of determining permeability using FMR is well suited for this. The results of this study have been published in the Journal of Magnetism and Magnetic Materials [24]. It is interesting to note that, though there is a change in magnetic anisotropy by stress annealing there is no significant change in other parameters like effective magnetization, damping and gyromagnetic ratio. I have carried out the FMR measurements and the data analysis related to it. The present study is a part of a larger NASA funded project which is aimed at obtaining a better understanding of the influence of morphology and local composition of the nanocomposite in amorphous and nanocrystalline phase on the magnetic properties of these materials.

In magnetic thin films the origin of the magnetic anisotropy is different. For single crys-

tal epitaxial films magnetocrystalline anisotropy can be observed. But due to the strain in the film from the substrate this anisotropy is affected. Strain also affects the damping in the system because large strain can lead to relaxation of the film which leads to defects in the film. We have studied the effect of different substrates ($MgGa_2O_4$ and $CoGa_2O_4$) on magnetite (Fe_3O_4) films, these studies have been published in the Journal of Applied Physics [25]. The magnetic anisotropy in these films can be significantly different from the bulk values. In Chapter 3 the magnetic anisotropy of magnetite thin films was investigated in detail, here we have shown that the magnetocrystalline anisotropy is indeed significantly smaller than the bulk value. Magnetite undergoes a metal-insulator transition at around 120 K known as the Verwey transition. This transition is named after Evert Verwey who made the connection between the changes of the physical properties (magnetic, electrical and thermal) and the structural transition [26]. The cubic phase of the crystal above the transition temperature transforms to monoclinic phase below the transition temperature. One of the most striking changes of the physical properties at the Verwey transition is the change in electrical conductivity as the material undergoes a metal to insulator transition. However, as the magnetocrystalline anisotropy originates from the crystal structure of the material, it is also affected by this transition. So in magnetite, the magnetic anisotropy can be altered reversibly by changing the temperature, in fact at a temperature about 10 K above the Verwey transition, known as isotropic point, the magnetic anisotropy becomes vanishingly small. This detailed study has been submitted to IEEE Transactions on Magnetics for publication. I have carried out the temperature dependent broadband FMR and the data analysis related to it.

In Chapter 4 we have studied how the anisotropy evolves in a polycrystalline $CdCr_2S_4$ paramagnetic film as the film goes through a paramagnetic to ferromagnetic phase transition as the temperature goes through the Curie temperature T_c. In this system the anisotropy is negligibly small in the paramagnetic state. As the film becomes ferromagnetic, the difference in resonance field between in-plane and out-of-plane increases indicating that a significant anisotropy starts to develop. This anisotropy originates from dipole-dipole interaction and the shape of the sample (thin film) and is called shape anisotropy. The damping in the paramagnetic state is not frequency

dependent, unlike in most ferromagnetic materials, this indicates that the relaxation process is different in paramagnets and can not be characterized by a Gilbert damping coefficient. In the ferromagnetic state the linewidth starts showing a linear frequency dependence, which is typical for ferromagnetic materials. The details of this study has been published in ACS applied electronic materials [27]. I have carried out the temperature dependent broadband FMR and the data analysis related to it. The first and the second authors are equivalent and shared between the authors who did material synthesis and the author who did material characterization. Chapter 5 concludes the findings in chapters 2-4.

In addition to the work compiled in this dissertation, high quality epitaxial iron films were studied in collaboration with Dr. Satoru Emori where we were able to show the importance of intraband scattering in the films. The detailed study has been published in the Physical Review Letters [28]. In another project on $NiFe_2O_4$ thin films, the influence of different anisotropy contributions on the spin seebeck effect was studied in collaboration with Dr. Arunava Gupta, Dr. Zbigniew Galazka, and Dr. Timo Kuschel, the studies have been published in the Applied Physics Letters [29]. In collaboration with Dr. Christian Kaiser from Western Digital company we investigated the interlayer exchange coupling in Co-Fe/Ru/Co-Fe trilayers using temperature dependent broadband FMR. The study has been published in the Physical Review Applied [30].

CHAPTER 2

BROADBAND CHARACTERIZATION OF STRESS INDUCED ANISOTROPY IN NANOCOMPOSITE $Co_{74.6}Fe_{2.7}Mn_{2.7}Nb_4Si_2B_{14}$

Abhishek Srivastava[1], Kayla Cole[1], Alicia Wadsworth[3], Thomas Burton[3], Claudia Mewes[2], Tim Mewes[1], Gregory B. Thompson[2], Ronald D. Noebe[2], Alex M. Leary[1]

1: Department of Physics and Astronomy, The University of Alabama, Tuscaloosa, AL 35487

2:Department of Metallurgical and Materials Engineering, The University of Alabama, Tuscaloosa, AL 35487, USA

3: Materials and Structures Division, NASA Glenn Research Center, Cleveland, OH 44135, USA

2.1 Abstract

We report on the broadband characterization of $Co_{74.6}Fe_{2.7}Mn_{2.7}Nb_4Si_2B_{14}$ (at %) melt-spun, soft magnetic alloy ribbons after various secondary processing treatments. Ribbons were investigated in the as-cast (melt-spun) condition, after annealing under stress at 50–200 MPa, and after transverse magnetic field (TMF) annealing. The magnetization dynamics of these materials have been studied from 10-60 GHz using ferromagnetic resonance (FMR). The in-plane uniaxial anisotropy was determined from the FMR data and permeability extracted for each condition. The permeability determined from broadband FMR was in good agreement with independently determined values using vibrating sample magnetometry and impedance spectrometry of toroidal cores. The effective damping parameter (α_{eff}) of all the samples was close to 0.015 except for the TMF sample, which showed higher damping, possibly due to two magnon scattering.

2.2 Introduction

Nanocomposite soft magnetic materials consist of nanocrystalline grains dispersed in an amorphous matrix [1]. The principle method for forming this type of material is to start with an amorphous precursor, usually melt spun ribbon, followed by thermal annealing, which partly devitrifies the material. One variation on this technique is to apply a stress to the ribbon while annealing the material, which provides an added benefit of being able to induce a controlled magnetic anisotropy. By changing the annealing conditions and the stress during annealing the magnitude of the induced anisotropy [2] as well as easy axis of the anisotropy can be tuned [3]. Co-rich nanocomposites exhibit an increased relative strain at fracture when compared to Fe-based nanocomposites [4], and have recently been shown to be excellent candidates for in-line stress-annealing techniques [1].

The permeability of nanocomposites is one of the key material parameters that determines their usefulness for inductive components in high power electronics, transformers and electrical motors. In this article, we report on permeability measurements of $Co_{74.6}Fe_{2.7}Mn_{2.7}Nb_4Si_2B_{14}$ (at%) after various annealing conditions using three different methods, vibrating sample magnetometry (VSM), impedance measurements of toroidal cores, and ferromagnetic resonance (FMR), and found the results to be in close agreement. This establishes FMR as an alternative method to determine the permeability of nanocomposite ribbons, while at the same time probing the high frequency dynamics of the materials. The method can be adapted for nondestructive permeability measurements by correcting for geometrical effects and might enable in-situ permeability measurement providing an advantage over conventional methods, which are destructive in nature.

High frequency damping characteristics are another important parameter for these types of soft magnetic materials when considered for applications like electromagnetic shielding [5] and high frequency power conversion [6]. Due to its high magnetic moment and soft magnetic properties, Co-base alloys, such as the $Co_{74.6}Fe_{2.7}Mn_{2.7}Nb_4Si_2B_{14}$ studied here, can also be used as a soft magnetic underlayer for magnetic flux concentration in perpendicular recording systems, for which the high frequency response is particularly important [7, 8]. We have extracted the ef-

fective damping parameter (α_{eff}) and inhomogeneous linewidth broadening (ΔH_0) from broadband FMR measurements, which show that both parameters are unaffected by stress annealing and are not significantly different from the as-cast samples. However, for samples annealed in a transverse magnetic field we find a significantly enhanced effective damping and inhomogeneous linewidth broadening.

2.3 Experimental techniques

Amorphous $Co_{74.6}Fe_{2.7}Mn_{2.7}Nb_4Si_2B_{14}$ (at%) ribbon, approximately 25 mm wide and 22 microns thick, was produced using a pilot-scale, planar-flow melt spin system. Melting and casting were performed in air under an inert gas-shrouded environment. In addition to studying the as-cast amorphous ribbon, two secondary annealing treatments were applied in air to the as-cast ribbon to produce different nanocomposite structures:

1. Transverse magnetic field annealing (TMF) at 540 °C for 1 hr with a 2 T magnetic field applied perpendicular to the ribbon long axis in the ribbon plane.

2. Stress annealing (SA) where sections of the ribbon were annealed while moving through a furnace at 560 °C under various tensions (50 to 200 MPa). Segments of ribbon underwent heating for approximately 5 seconds during this in-line anneal.

The saturation magnetization, M_s, of the as-cast and annealed materials were measured using a Lake Shore 7400 Vibrating Sample Magnetometer (VSM). Density of the as-cast and annealed material is $\rho = 8.35 \pm 0.05$ g/cc and accuracy of specific magnetization was within ± 1 Am^2/kg for the $\sim$20 mg samples, resulting in a 1.7% accuracy for the measured induction values (B) from the VSM data. FMR measurements were performed on a custom system that utilizes a coplanar waveguide (CPW), capable of exciting the sample with a microwave field between 1 to 65 GHz [9]. FMR measurements used a fixed microwave frequency and swept the external applied field to obtain resonance in the sample. Power transmitted through the sample located on the CPW is detected using a Schottky diode with a lock-in technique by adding a small modulation field to

the applied field [10]. For the measurements on the nanocomposite ribbons, the modulation frequency was $f_{mod} = 800$ Hz and the modulation field, $\mu_0 H_{mod}$, was varied linearly with microwave frequency from 2 mT at 10 GHz to 4 mT at 56 GHz.

Three different techniques were used to measure magnetic anisotropy and permeability; impedance measurements on wound cores, in plane FMR using 6 mm discs, and in plane VSM using 3 mm discs. Impedance spectra of TMF and SA toroidal cores with cross section A_c and path length ℓ, were wound with two $N = 50$ turn bifilar windings and were measured using a Keysight E4990A Impedance Analyzer. Material permeability was determined using the measured equivalent series inductance at 10 kHz from the primary winding with the secondary winding open (L_o) and shorted (L_s). The measured inductance $L_m = L_o - L_s$ corrects for the leakage effects and the relative permeability μ_r is obtained from $L_m = N^2 A_c \mu_r \mu_o / \ell$ with μ_0 equal to the permeability of free space. In-plane FMR and VSM measurements used disc samples punched from ribbons and mounted to the flat end of a glass rod that is free to rotate about its axis by a servo motor. Figure 2.1 describes the coordinate system of the large, quasi-DC applied field that was swept over the resonance field at a fixed frequency in the FMR and swept between positive and negative values that saturated the disc sample in the VSM to measure hysteresis. Both in plane techniques varied the field angle θ to achieve a full 360° rotation with 5° increments, where $\theta = 0°$ orients the quasi-DC field parallel to the long axis of the ribbon, which was also the direction of applied stress during stress annealing. Anisotropy values from the FMR and VSM techniques were derived from measured values as described below.

2.4 Results

Figure 2.2 (a) shows a typical FMR spectrum at $\theta = 0°$ and a fit using the first derivative of a Lorentzian with both absorptive and dispersive contributions [11, 12]. From this fit, the resonance field, H_{res}, and the linewidth, ΔH, are determined. In this example, the resonance field $\mu_0 H_{res}$ = 1.1 T and linewidth $\mu_0 \Delta H_{PP}$ = 44.3 mT for a 3 mT modulation field at 800 Hz. By measuring the H_{res} over a broad frequency range one obtains the data shown in figure 2.2 (b). This data is

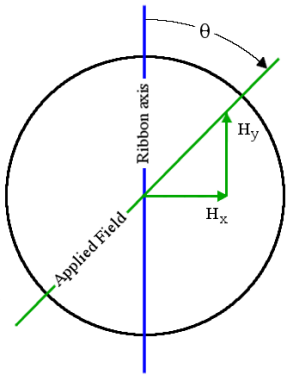

Figure 2.1: Coordinate system describing the applied DC field for in-plane disc measurements.

well described by the Kittel equation 2.1 for a material with a uniaxial in-plane anisotropy, K_u, measured along the hard-axis [13, 14].

$$f = \mu_0 \cdot \gamma' \sqrt{\left[H_{res} - H_u\right]\left[H_{res} + M_{eff}\right]} \tag{2.1}$$

Where M_{eff} is the effective magnetization, the reduced gyromagnetic ratio $\gamma' = \frac{\gamma}{2\pi}$, and the in-plane uniaxial anisotropy field $H_u = \frac{2K_u}{\mu_0 M_s}$ where K_u is the uniaxial anisotropy constant and M_s is the saturation magnetization . The effective magnetization accounts for both the shape anisotropy of the disc and the perpendicular anisotropy and is given by

$$M_{eff} = M_s - \frac{2K_\perp}{\mu_0 M_s} \tag{2.2}$$

where M_s is the saturation magnetization and $K_\perp$ is the out-of-plane perpendicular anisotropy of the ribbon. For samples with $K_\perp = 0$ the effective magnetization is equal to the saturation magnetization of the sample. The values of M_{eff} and γ', obtained by fitting the experimental data using equation 2.1, are summarized in Table 2.1 and shown in figure 2.3. The effective magnetization (figure 2.3 (a)) for the as-cast sample is slightly higher than the stress annealed samples and no significant dependence on the stress during annealing is observed. Also, the gyromagnetic ratio (figure 2.3(b)) remained constant within the error margin for all samples.

While the fit of broadband FMR data also results in a parameter for the anisotropy field, H_u,

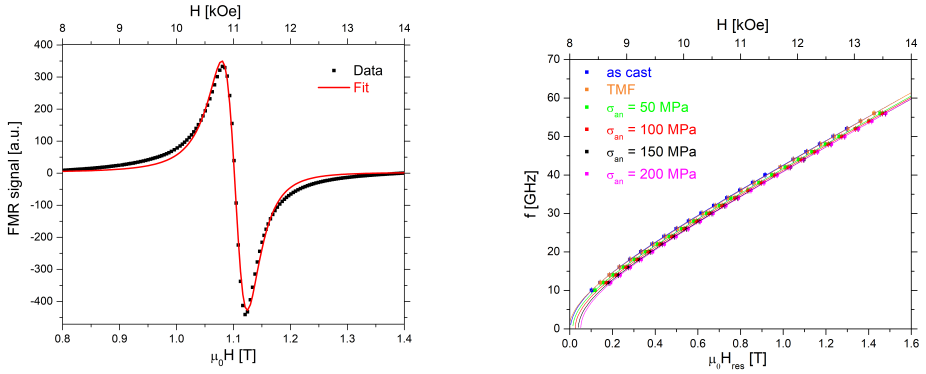

(a) (b)

Figure 2.2: a) Field swept FMR spectrum measured at 46 GHz for a sample stress annealed at 100 MPa. b) Frequency dependence of FMR resonance field of all the samples. The continuous lines represent the fit to the experimental data using equation 2.1.

in the sample, this value should only be considered a rough estimate of the anisotropy field. For completeness these values are listed in Table 2.1 with the label 'Kittel'. Because the measurements were only carried out with the field applied along the spin-casting direction, no conclusion regarding the symmetry of the anisotropy can be derived from those measurements alone. However, as can be seen in figure 2.2 (b) the ferromagnetic resonance frequency drops to zero at finite positive fields indicating that this is a hard axis of the sample. Furthermore, we note that the magnitude of H_u, determined in this fashion, will sensitively depend on the relative alignment of the field with respect to the anisotropy axis of the sample. This systematic error is not included in the error margins in Table 2.1, which are based solely on the statistical error of the anisotropy field. The correlation of the different fit parameters in equation 2.1 further adds to the uncertainty of this value. Thus in order to obtain precise values for H_u, we have performed in-plane angle dependent FMR measurements for all samples, which clearly show the uniaxial nature of the anisotropy.

@ 300 K	as-cast	stress annealed at 50 MPa	stress annealed at 100 MPa	stress annealed at 150 MPa	stress annealed at 200 MPa	annealed in TMF
$\mu_0 M_{eff}$[T]	1.01 ± 0.01	0.92 ± 0.03	0.91 ± 0.05	0.91 ± 0.03	0.91 ± 0.02	0.93 ± 0.01
γ'[GHz/T]	30.08 ± 0.07	30.3 ± 0.2	30.26 ± 0.03	30.21 ± 0.02	30.36 ± 0.01	30.50 ± 0.05
$\mu_0 H_u$(Kittel)[mT]	4 ± 1	14 ± 3	25.6 ± 0.6	39.9 ± 0.4	51 ± 3	-3 ± 1
$\mu_0 H_u$(in-plane rotation)[mT]	0 ± 2	13.6± 0.1	26.3 ± 0.2	36.2 ± 0.2	41.1 ± 0.4	0 ± 4

Table 2.1: Parameters extracted from Kittel plot

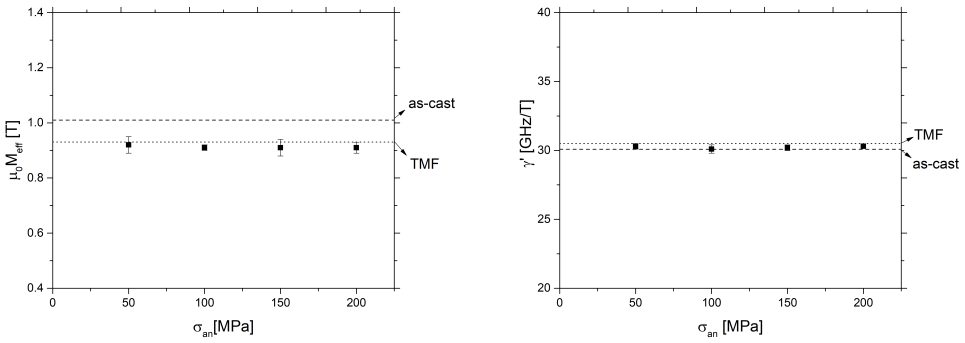

(a) (b)

Figure 2.3: (a) Effective magnetization, M_{eff}, and (b) the reduced gyromagnetic ratio, γ', extracted from broadband FMR measurements for all the samples. The data points represent the different stress annealed conditions, the dashed horizontal line represents the corresponding parameters of the as-cast ribbon, and dotted line corresponds to the ribbon sample annealed in a transverse magnetic field (TMF).

The nature of the magnetic anisotropy becomes evident by varying θ during FMR measurements. For the as-cast and TMF samples, the FMR technique shows no significant in-plane anisotropy, as is evident in figure 2.4 (a) and (b), respectively. Stress annealed samples do show clear minima in the angular variation of the resonance field, as shown in figures 2.4 (c)-(f), that indicate an easy direction near $\theta = 90°$. Assuming that the magnetization is aligned with the externally applied field for all angles, i.e. $\theta_M = \theta$ and for $M_s > H_{res} \gg H_u$ an approximate analytic expression for the in-plane angular dependence of the resonance field is given by [14–16]:

$$H_{res} = H_0 - H'_u \cos(2(\theta_M - \theta_0)) \tag{2.3}$$

In this equation the angle of the magnetization, θ_M, is defined relative to the easy axis located at θ_0. As noted above, the easy axis for the stress annealed samples is perpendicular to the direction of applied tensile stress, i.e., $\theta_0 = 90°$. A fit of the experimental data using equation 2.3 is shown in figures 2.4 (c)-(f). While the parameter H'_u in equation (2.3) is often identified as the uniaxial anisotropy of the material, the assumptions underlying the derivation of this equation imply that $H'_u \neq H_u$, where H_u is the anisotropy field introduced in equation (2.1)[14]. However, the two

quantities are related by the following expressions:

$$
\begin{aligned}
H_u &= \frac{1}{2}\left(-b+\sqrt{b^2-4c}\right) \quad \text{with} \\
b &= \frac{1}{8}\left(6\tilde{H}_u + 2M_{eff}\right), \\
c &= \frac{1}{8}\left(\tilde{H}_u^2 - 4\frac{f^2}{\gamma'^2} - M_{eff}^2\right) \quad \text{and} \\
\tilde{H}_u &= \sqrt{M_{eff}^2 + 4\frac{f^2}{\gamma'^2}} - 4H_u'
\end{aligned}
\tag{2.4}
$$

Therefore by fitting the in-plane angular variation of resonance field, H_{res}, as a function of the direction of external magnetic field, using equations (2.3) and (2.4) we obtain the uniaxial anisotropy field in the material, H_u. These values are indicated in figure 2.4 and listed in Table 2.1 with the identifier 'in-plane rotation', the values $\mu_0 H_u$ range from 13.6 mT for the sample stress annealed at 50 MPa to 41.1 mT for the sample stress annealed at 200 MPa. The data in Table 2.1 also show that the statistical error margins of the uniaxial anisotropy field obtained from in-plane angle dependent measurements for the stress annealed samples is significantly lower than those obtained from frequency dependent data.

Broadband ferromagnetic resonance measurements also provide valuable information about the relaxation in the samples [17]. The analysis of this information is based on the frequency dependence of the linewidth, shown in figure 2.5. Based on Suhl's formula [18], which is valid when $\theta = \theta_M$, the frequency dependence of the linewidth is [19–21]:

$$
\Delta H = \Delta H_0 + \frac{2}{\sqrt{3}} \cdot \alpha_{eff} \cdot \frac{f}{\gamma'} \tag{2.5}
$$

Here, f is the microwave frequency, α_{eff} is the effective Gilbert damping parameter, ΔH is the peak-to-peak linewidth, ΔH_0 is the linewidth extrapolated to zero frequency, and γ' is the reduced gyromagnetic ratio. The parameters extracted from linewidth vs. frequency data are shown in figure 2.6. The damping coefficient, α_{eff} , for the as-cast and strain annealed samples are of the same order of magnitude (see figure 2.6 (b)) and Table 2.2) indicating that relaxation is not af-

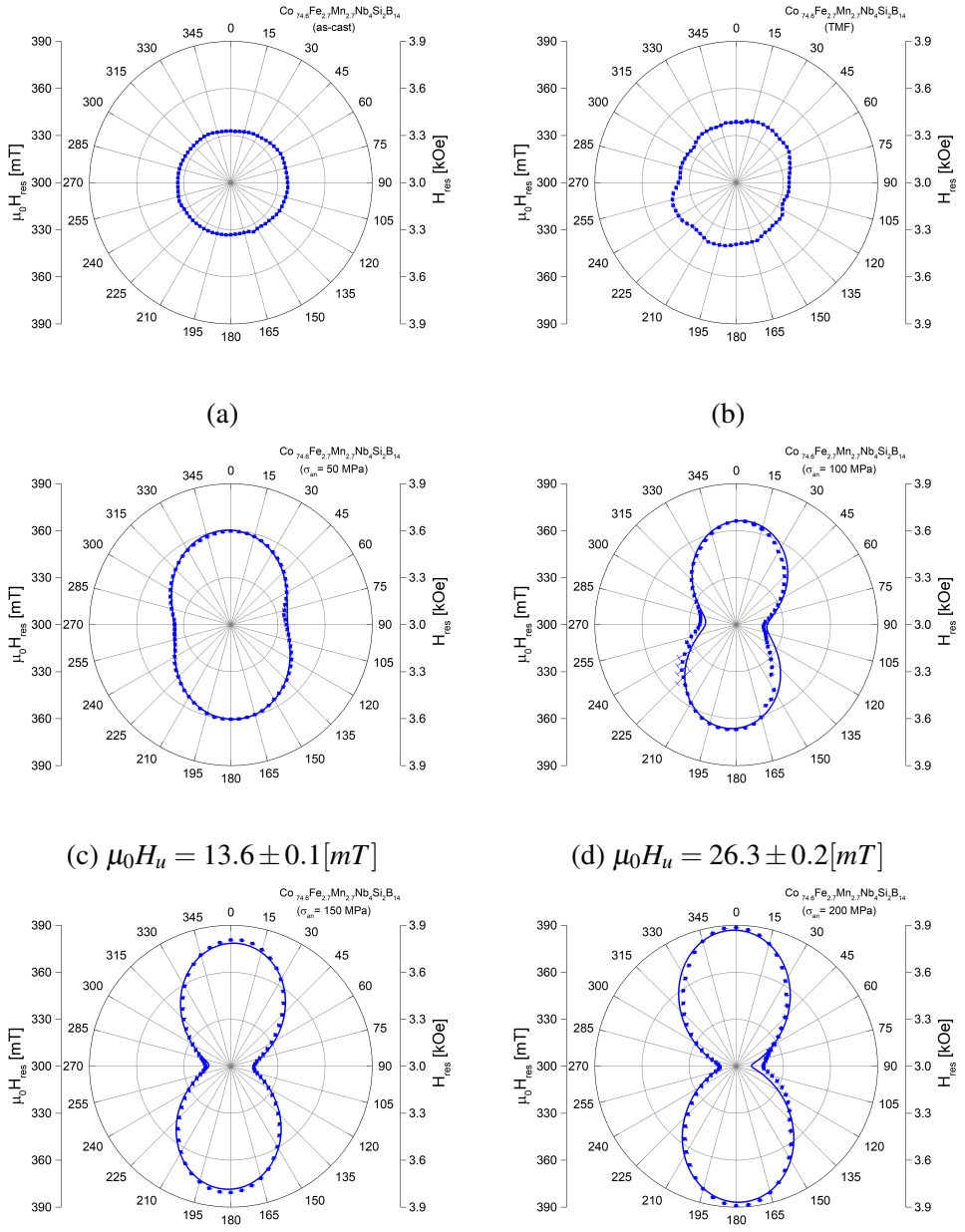

(a) (b)

(c) $\mu_0 H_u = 13.6 \pm 0.1[mT]$ (d) $\mu_0 H_u = 26.3 \pm 0.2[mT]$

(e) $\mu_0 H_u = 36.2 \pm 0.2[mT]$ (f) $\mu_0 H_u = 41.1 \pm 0.4[mT]$

Figure 2.4: In-plane angular variation of resonance field at 20 GHz of a) as-cast, b) annealed in transverse magnetic field (TMF), c) stress annealed at 50 MPa, d) 100 MPa, e) 150 MPa and f) 200 MPa. Zero degree corresponds to the spin-casting direction and also the stress axis in SA samples. The experimental data is shown as blue squares, and the fit is shown as a continuous line.

fected by stress annealing. Moreover, similar values of ΔH_0 (see figure 2.6 (a) and Table 2.2) suggest that the magnetic inhomogeneity also does not depend on stress annealing of the material. However, both values are significantly different in the case of the transverse magnetic field annealed sample (Table 2.2). A nonlinear frequency dependence of the linewidth as observed for the TMF sample (see figure 2.5) is indicative of a strong two-magnon scattering [14, 22].

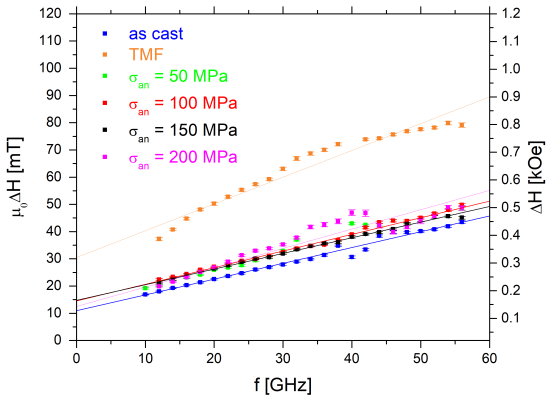

Figure 2.5: Frequency dependence of the FMR linewidth of all $Co_{74.6}Fe_{2.7}Mn_{2.7}Nb_4Si_2B_{14}$ samples. The continuous line is fit to the data using equation 2.5

.

@ 300 K	as-cast	stress annealed at 50 MPa	stress annealed at 100 MPa	stress annealed at 150 MPa	stress annealed at 200 MPa	annealed in TMF
$\mu_0\Delta H_0$[mT]	10.9 ± 0.4	13.2 ± 0.7	12.9 ± 0.6	19.2 ± 0.7	17.8 ± 0.6	30 ± 2
α	$0.0152 \pm$ 4E-4	$0.0164 \pm$ 4E-4	$0.0159 \pm$ 3E-4	$0.0151 \pm$ 2E-4	$0.019 \pm$ 1E-3	$0.026 \pm$1E-3

Table 2.2: Parameters extracted from linewidth vs frequency data

The saturation induction, $B_s = \mu_0 M_s$, measured using VSM, of the as-cast ribbon, the TMF, and 100 MPa SA samples were 1.01 T, 0.94 T, 0.99 T, respectively. Saturation induction is known to decrease during annealing, as previously reported for this class of Co-rich materials [23], and longer annealing times above the primary crystallization temperature $\simeq$ 420 °C, produce lower induction materials compared to shorter annealing times. Thus, the 1 hour treatment at 540 °C for the TMF sample significantly reduces the saturation induction compared to the as-cast material, while there is very little change after strain annealing, since the sample was at temperature for only about 5 seconds. The saturation values derived from FMR data (Table 2.1) agree

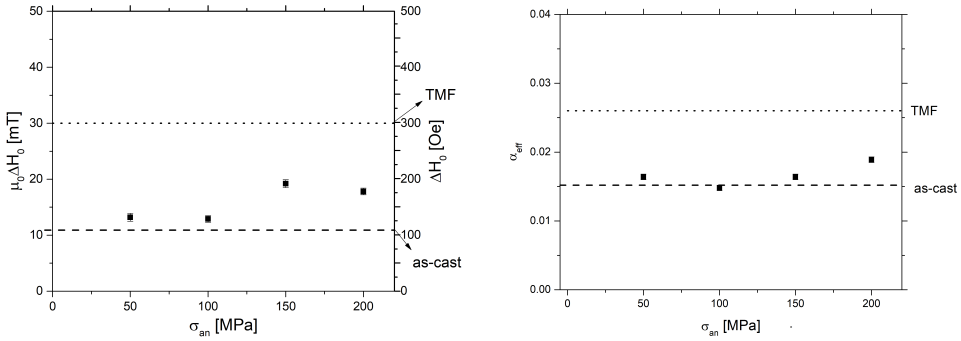

(a) (b)

Figure 2.6: (a) Linewidth extrapolated to zero field and (b) effective damping constant extracted from the frequency dependence of linewidth, obtained from broadband FMR measurements for the as-cast $Co_{74.6}Fe_{2.7}Mn_{2.7}Nb_4Si_2B_{14}$ alloy and after different annealing treatments. The data points represent the different stress annealed conditions, the dashed horizontal line represents the corresponding parameters of the as-cast ribbon, and dotted line corresponds to the ribbon sample annealed in a transverse magnetic field (TMF).

well with B_s values measured using the VSM. It is worth mentioning in this context that FMR measurements do not require knowledge of the volume or mass of the sample but instead solely rely on precise measurements of the resonance field. Magnetic anisotropy can also be determined from torque measurements in a VSM equipped with at least two coils to detect orthogonal magnetization components [24]. The torque τ is produced by the magnetization perpendicular to the effective field that accounts for shape anisotropy as $\tau = \mu_0 M_\perp H_{eff}$. For magnetization oriented at θ_M from a uniaxial easy axis in the same plane, the energy is [25] $E_a = K_0 + K_{u,1}\sin^2(\theta_M) + K_{u,2}\sin^4(\theta_M) + \cdots$ and the anisotropy constants can be derived by fitting the torque curve to a Fourier series. Anisotropy constants can also be calculated from a single magnetization curve if H_{eff} accounts for shape anisotropy [26]. While shape anisotropy is significant in the disc samples described here favoring an in-plane orientation of the magnetization over an out-of-plane orientation, closure domains near the surface can stabilize bulk domains with significant out of plane orientations. Furthermore the shape anisotropy is isotropic in the plane of the disk. The proposed VSM technique does not require direct measurement of the demagnetizing fields and follows from the magnetic energy, given as:

$$E = E_{ex} + E_a + E_{sh} - \mathbf{M} \cdot \mathbf{H}. \tag{2.6}$$

where E_{ex} is exchange energy, E_a is anisotropy energy, E_{sh} is energy due to shape anisotropy and last term is the Zeeman energy.

In randomly oriented nanocomposites where the magnetocrystalline anisotropy is effectively averaged, the exchange energy E_{ex} is isotropic and the shape anisotropy E_{sh} for the disc geometry of our sample is also isotropic in the ribbon plane. Consequently, the induced anisotropy energy K_u can be measured using the VSM by comparing the susceptibility ($\chi = \frac{dM}{dH}$) of discs magnetized across different in-plane directions as in equation 2.7, which assumes constant χ to saturation.

$$\frac{1}{\chi_{hard}} - \frac{1}{\chi_{easy}} = \frac{1}{M_s}(H_{k,hard} - H_{k,easy}) \tag{2.7}$$

As all the energy terms are isotropic in the plane of the disc for $H \to 0$ the energy difference between easy and hard axis, $E_{hard} - E_{easy} = \Delta K_u$. With $\Delta K_u = \frac{1}{2}\mu_0 M_s(H_{k,hard} - H_{k,easy})$, one has

$$\Delta K_u = \frac{\mu_0 M_s^2}{2}\left(\frac{1}{\chi_{hard}} - \frac{1}{\chi_{easy}}\right). \tag{2.8}$$

With the permeability of free space $\mu_0 = 4\pi \times 10^{-7}\ \mathrm{m \cdot kg/s^2 \cdot A^2}$. The saturation magnetization $M_s = \rho \cdot \sigma_s$ (σ_s: mass magnetization) is determined by saddling the sample between the VSM poles and applying a saturating field. Small sample movement from the initial saddled position, as θ varies, can be detected by monitoring $\sigma_s(\theta)$ under sufficiently high fields. This misalignment creates an error in the measured magnetization that can be corrected by scaling the measured data by the saddled, saturated value. Figure 2.7 (a) shows σ vs H measurements along the easy and hard directions of an SA 100 MPa sample. The applied field at each θ varies as $H = \sqrt{H_x^2 + H_y^2}$ as shown in figure 2.1 and χ at each radial field position on the positive portion of the hysteresis loop can be plotted to show the K_u symmetry in the material. Figure 2.7 (b) and (c) show radial susceptibility plots of 100 MPa SA and TMF samples, respectively, where

the ribbon axis runs parallel to the $\theta = 0$ direction. Darker colors correspond to lower permeability with the black regions illustrating the saturating fields with respect to θ. Both materials show uniaxial symmetry and the SA material requires a higher saturating field along the ribbon axis direction compared to the TMF material.

Equation 2.8 is only valid if the angle dependent energy is dominated by the induced anisotropy. This is checked by comparing the energy product $M(\theta)H(\theta)$ where M is the measured magnetization of the sample and H is the external applied field. If $M(\theta)H(\theta)$ is proportional to $\chi_{hard} + \Delta\chi \cdot \sin^2\theta$ at a fixed H value, the conditions required for equation 2.8 are satisfied. Consequently the susceptibilities for equation 2.8 can be determined by fitting $\chi_{hard} + \Delta\chi \cdot \sin^2\theta$ function to the χ vs θ values at $H \to 0$, where $\Delta\chi = \chi_{easy} - \chi_{hard}$.

Figure 2.8 shows fits to data at 100 A/m that yield $\chi_{hard} = 82.0 \pm 0.6$ and $\chi_{easy} = 117.0 \pm 0.6$ for the TMF sample and $\chi_{hard} = 27.5 \pm 0.5$ and $\chi_{easy} = 106.0 \pm 0.5$ for the 100 MPa SA sample. The corresponding K_u values are 1294 ± 40 J/m^3 for the TMF and 10475 ± 350 J/m^3 for the 100 MPa SA samples. The susceptibility measured along the easy axis is slightly lower than the maximum effective susceptibility expected for the disc shaped samples $\chi_{easy,max} = \frac{1}{N_{||}} = 143$, where $N_{||} = N_{xx} = N_{yy} = 0.007$ is the in-plane component of the demagnetizing tensor . This is expected as defects in the samples will reduce the measured susceptibility. Taking $\mu_r = 1 + \frac{M_s}{H_u} \approx \frac{M_s}{H_u}$ yields $\mu_r = 274 \pm 15$ for the TMF sample and $\mu_r = 37.2 \pm 1.8$ for the 100 MPa SA sample, as derived using the VSM technique. The relative permeability value is an intrinsic material property.

relative permeability at 300K	stress annealed at 50 MPa	stress annealed at 100 MPa	stress annealed at 150 MPa	stress annealed at 200 MPa	stress annealed at 250 MPa	TMF
Toroid method	73 ± 4	43 ± 2	32 ± 2	26 ± 1	23 ± 1	262 ± 5
VSM method	-	37 ± 2	-	-	-	274 ± 15
FMR method	69 ± 2	36 ± 2	26 ± 1	23 ± 1	-	-

Table 2.3: Permeability obtained using the toroid method, vibrating sample magnetometry (VSM), and ferromagnetic resonance (FMR). In the case of the FMR results, the effective magnetization of the respective sample obtained using broadband FMR was used to calculate the value listed in the table.

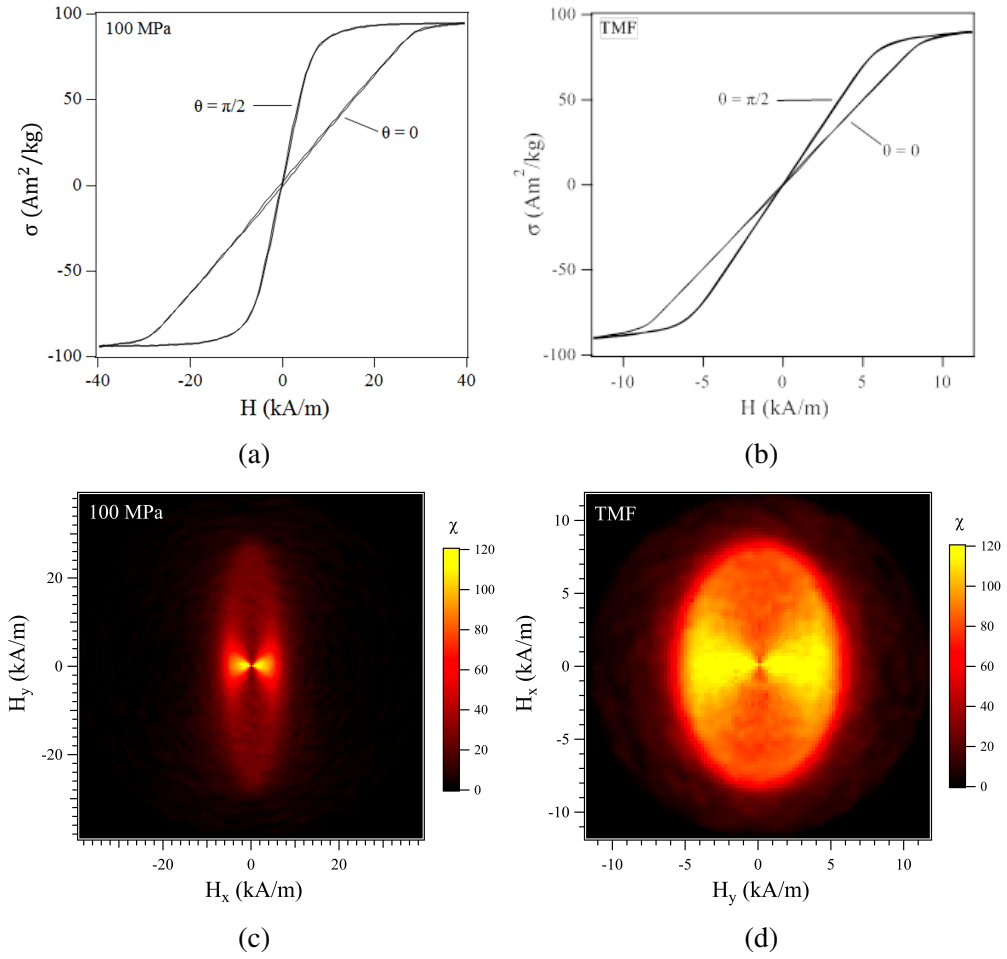

Figure 2.7: Hysteresis curves from a) 100 MPa SA sample and b) TMF sample measured with the field applied along the easy ($\theta = \frac{\pi}{2}$) and hard directions ($\theta = 0$). Radial susceptibility χ plots for c) SA and d) TMF samples, which show the symmetry of the induced anisotropy and saturating fields.

2.5 Discussion

The influence of the stress level during the annealing process on the uniaxial anisotropy field for $Co_{74.6}Fe_{2.7}Mn_{2.7}Nb_4Si_2B_{14}$ as determined using in-plane angle dependent FMR, is shown in figure 2.9. For comparison, the values determined from broadband FMR measurements (black), are also shown. As discussed earlier, the values from broadband FMR can only serve as a rough estimate of the true anisotropy as they not only have larger statistical error margins, but also suffer from systematical errors like misalignment of the sample. Thus for the following discussion we focus on the uniaxial anisotropy field values, H_u, determined from in-plane rotation measure-

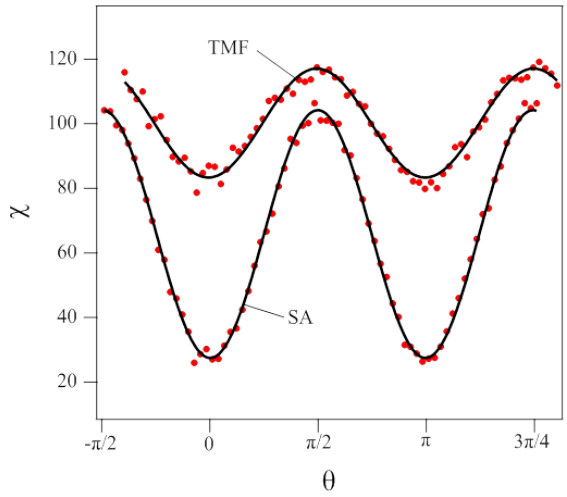

Figure 2.8: Angle dependent susceptibility χ, measured using VSM at H = 100 A/m for $Co_{74.6}Fe_{2.7}Mn_{2.7}Nb_4Si_2B_{14}$ TMF and 100 MPa SA samples. Fits correspond to $\chi_{hard} + \Delta\chi \cdot \sin^2\theta$.

ments.

For $Co_{74.6}Fe_{2.7}Mn_{2.7}Nb_4Si_2B_{14}$ the uniaxial magnetic anisotropy increases with increasing stress during the annealing process, at least over the levels of stress investigated. Thus the magnetic anisotropy induced by stress annealing in these nanocomposite ribbons can be tuned over a wide range. In typical applications the relative magnetic permeability, μ_r, of the material in small fields applied along the hard axis is of particular importance. In this configuration one expects the magnetization reversal to be determined by rotation of the magnetization from the easy axis of the material toward the field direction [27, 28], resulting in a nearly constant permeability up to saturation, which in this model occurs at $H_s = H_u$. With this, one can determine the permeability of the samples using FMR measurement as $\mu_r = 1 + \frac{M_{eff}}{H_u}$. The resulting permeabilities are shown in figure 2.10 and in Table 2.3 in comparison with the results from VSM and the toroid method. The permeability in the SA samples determined using the toroid method is systematically higher than those determined using the other methods. Possible reasons for this include the assumption of a constant permeability until saturation that is used for both the VSM and FMR analyses and any stress induced in the core during winding. This stress can lead to a permeability measured using the toroid method that is different from the intrinsic value of the ribbon material [29, 30].

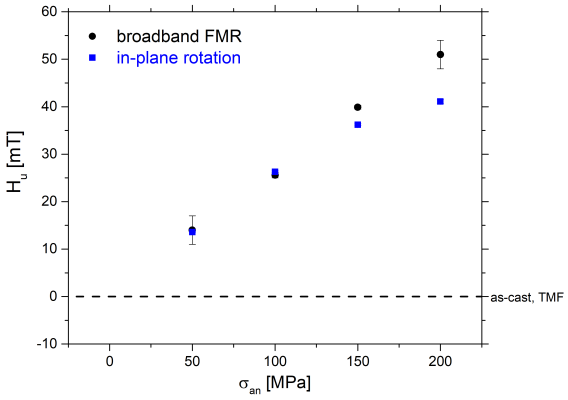

Figure 2.9: Dependence of the uniaxial anisotropy field, H_u, on the stress during annealing. Data obtained from broadband FMR measurements are shown as black symbols whereas the more precise data obtained from in-plane angle dependent measurements are shown in blue.

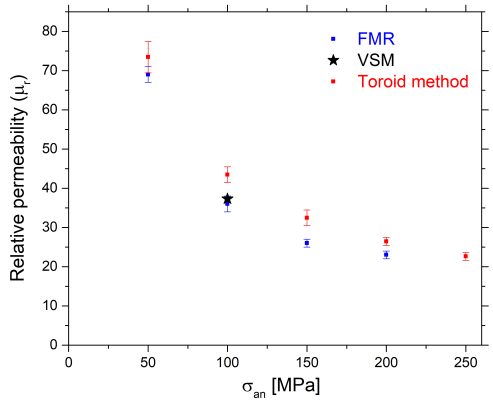

Figure 2.10: Comparison of the relative permeability as a function of the stress during annealing determined using the toroid method, VSM, and using the anisotropy field (H_u) obtained from FMR, assuming $M_s = M_{eff}$.

Given these possible issues, the agreement between the different methods is actually very good.

2.6 Conclusion

In summary we have studied $Co_{74.6}Fe_{2.7}Mn_{2.7}Nb_4Si_2B_{14}$, a soft magnetic alloy in the as-cast (melt-spun) condition, after stress annealing at 50-200 MPa and after annealing in a transverse magnetic field. In addition to the established toroid and VSM methods we have shown that

broadband FMR provides an alternative method to determine the permeability of soft magnetic materials. Similar to the VSM method the FMR method is based on a linear approach to saturation or constant susceptibility.

By combining frequency dependent FMR measurements with in-plane angle dependent measurements we were able to achieve good agreement of the extracted susceptibility with the other methods.

In addition, broadband FMR also provides precise information regarding the effective magnetization, gyromagnetic ratio and damping of the material. The damping parameter plays a particularly important role for the potential use of these materials in high frequency applications.

2.7 Acknowledgement

The authors gratefully acknowledge funding for this research under the NASA Grant NASA CAN80NSSC18M0023. Additional support for this work came from the Advanced Air Transport Technology Project in the NASA Advanced Air Vehicles Program. R.D.N and A.M.L also acknowledge useful discussions and experimental support from K. Beyerly, R. Bowman, V. Keylin, and G. Feichter.

2.8 References

[1] K. Byerly, P. Ohodnicki, S. Moon, A. Leary, V. Keylin, M. McHenry, S. Simizu, R. Beddingfield, Y. Yu, G. Feichter, *et al.*, *Metal amorphous nanocomposite (MANC) alloy cores with spatially tuned permeability for advanced power magnetics applications*, JOM **70**, 879 (2018).

[2] A. Leary, V. Keylin, P. Ohodnicki, and M. McHenry, *Stress induced anisotropy in CoFeMn soft magnetic nanocomposites*, Journal of Applied Physics **117**, 17A338 (2015).

[3] O. Nielsen and H. Nielsen, *Magnetic anisotropy in* $Co_{73}Mo_2Si_{15}B_{10}$ *and* $(Co_{0.89}Fe_{0.11})_{72}Mo_3Si_{15}B_{10}$ *metallic glasses, induced by stress-annealing*, Journal of Magnetism and Magnetic Materials **22**, 21 (1980).

[4] T. Heil, K. Wahl, A. Lewis, J. Mattison, and M. Willard, *Nanocrystalline soft magnetic ribbons with high relative strain at fracture*, Applied physics letters **90**, 212508 (2007).

[5] Y. Yang, B. Liu, D. Tang, B. Zhang, M. Lu, and H. Lu, *Influence of the magnetic field annealing on the extrinsic damping of FeCoB soft magnetic films*, Journal of Applied Physics **108**, 073902 (2010).

[6] A. M. Leary, P. R. Ohodnicki, and M. E. McHenry, *Soft magnetic materials in high-frequency, high-power conversion applications*, JOM **64**, 772 (2012).

[7] H. Okumura, D. Twisselmann, R. D. McMichael, M. Huang, Y. Hsu, D. Laughlin, and M. McHenry, *Magnetic and structural characterization and ferromagnetic resonance study of thin film HITPERM soft magnetic materials for data storage applications*, Journal of Applied Physics **93**, 6528 (2003).

[8] C.-K. Lim, E.-S. Kim, and H.-S. Oh, *Perpendicular magnetic recording medium with controlled damping property of soft magnetic underlayer*, US Patent App. 11/657,595 (2007).

[9] B. Khodadadi, J. B. Mohammadi, J. M. Jones, A. Srivastava, C. Mewes, T. Mewes, and C. Kaiser, *Interlayer Exchange Coupling in Asymmetric Co-Fe/Ru/Co-Fe Trilayers Investigated with Broadband Temperature-Dependent Ferromagnetic Resonance*, Physical Review Applied **8**, 014024 (2017).

[10] C. P. Poole, *Electron spin resonance: a comprehensive treatise on experimental techniques* (Courier Corporation, 1996).

[11] C. J. Oates, F. Y. Ogrin, S. L. Lee, P. C. Riedi, G. M. Smith, and T. Thomson, *High field ferromagnetic resonance measurements of the anisotropy field of longitudinal recording thin-film media*, Journal of Applied Physics **91**, 1417 (2002).

[12] N. Pachauri, B. Khodadadi, A. V. Singh, J. B. Mohammadi, R. L. Martens, P. R. LeClair, C. Mewes, T. Mewes, and A. Gupta, *A comprehensive study of ferromagnetic resonance and structural properties of iron-rich nickel ferrite (*$Ni_xFe_{3-x}O_4, x < 1$*) films grown by chemical vapor deposition*, Journal of Magnetism and Magnetic Materials **417**, 137 (2016).

[13] C. Kittel, *On the theory of ferromagnetic resonance absorption*, Phys. Rev. **73**, 155 (1948).

[14] J. Beik Mohammadi, J. M. Jones, S. Paul, B. Khodadadi, C. K. A. Mewes, T. Mewes, and C. Kaiser, *Broadband ferromagnetic resonance characterization of anisotropies and relaxation in exchange-biased IrMn/CoFe bilayers*, Phys. Rev. B **95**, 064414 (2017).

[15] H. Xi, K. R. Mountfield, and R. M. White, *Ferromagnetic resonance studies of exchange biasing in $Ni_{81}Fe_{19}/Pt_{10}Mn_{90}$ bilayers*, Journal of Applied Physics **87**, 4367 (2000).

[16] A. Layadi, W. Cain, J. . Lee, and J. Artman, *Investigation of anisotropy by ferromagnetic resonance (FMR) in exchange-coupled bilayer films*, IEEE Transactions on Magnetics **23**, 2993 (1987).

[17] C. K. Mewes and T. Mewes, *Relaxation in magnetic materials for spintronics*, Handbook of Nanomagnetism , 71 (2015).

[18] H. Suhl, *Ferromagnetic resonance in nickel ferrite between one and two kilomegacycles*, Phys. Rev. **97**, 555 (1955).

[19] B. Heinrich, J. F. Cochran, and R. Hasegawa, *FMR linebroadening in metals due to two-magnon scattering*, Journal of Applied Physics **57**, 3690 (1985).

[20] Z. Celinski and B. Heinrich, *Ferromagnetic resonance linewidth of Fe ultrathin films grown on a bcc Cu substrate*, Journal of Applied Physics **70**, 5935 (1991).

[21] T. D. Rossing, *Resonance linewidth and anisotropy variation in thin films*, Journal of Applied Physics **34**, 995 (1963).

[22] R. Arias and D. Mills, *Extrinsic contributions to the ferromagnetic resonance response of ultrathin films*, Physical review B **60**, 7395 (1999).

[23] A. M. Leary, P. R. Ohodnicki, M. E. McHenry, V. Keylin, J. Huth, and S. J. Kernion, *Tunable anisotropy of Co-based nanocomposites for magnetic field sensing and inductor applications*, US Patent 10,168,392 (2019).

[24] J. L. B.C. Dodrill and J. Krausen, *Magnetic anisotropy: Measurements with a vector vibrating sample magnetometer*, Application Note, Lakeshore Cryogenics (2004).

[25] J. Mohammadi, K. Cole, T. Mewes, and C. Mewes, *Inhomogeneous perpendicular magnetic anisotropy as a source of higher-order quasistatic and dynamic anisotropies*, Physical Review B **97**, 014434 (2018).

[26] W. Sucksmith and J. E. Thompson, *The magnetic anisotropy of Cobalt*, Proceedings of the Royal Society of London. Series A. Mathematical and Physical Sciences **225**, 362 (1954).

[27] E. C. Stoner and E. P. Wohlfarth, *A mechanism of magnetic hysteresis in heterogeneous alloys*, Philosophical Transactions of the Royal Society of London. Series A, Mathematical and Physical Sciences **240**, 599 (1948).

[28] G. Herzer, *Modern soft magnets: Amorphous and nanocrystalline materials*, Acta Materialia **61**, 718 (2013).

[29] F. Luborsky and J. Becker, *Strain-induced anisotropy in amorphous alloys and the effect of toroid diameter on magnetic properties*, IEEE Transactions on Magnetics **15**, 1939 (1979).

[30] W. Grimmond, A. J. Moses, and P. C. Ling, *Geometrical factors affecting magnetic properties of wound toroidal cores*, IEEE Transactions on Magnetics **25**, 2686 (1989).

CHAPTER 3

FERROMAGNETIC RESONANCE STUDY OF THE VERWEY PHASE TRANSITION OF MAGNETITE THIN FILM ON $MgGa_2O_4$ (001)

Abhishek Srivastava[1], Amit V. Singh[2], Jamileh Beik Mohammadi[3], Claudia Mewes[2], Arunava Gupta[2], Tim Mewes[1]

1: Department of Physics and Astronomy, The University of Alabama, Tuscaloosa, AL 35487

2: Department of Chemistry and Biochemistry, The University of Alabama, Tuscaloosa, AL 35487

3: Department of Physics, Loyola University of New Orleans, New Orleans, LA 70018

3.1 Abstract

We report on temperature-dependent broadband ferromagnetic resonance studies of magnetite (Fe_3O_4) film of thickness 30 nm grown on magnesium gallate ($MgGa_2O_4(001)$) single crystal substrate by pulsed laser deposition. The isotropic point, i.e. the temperature at which magnetocrystalline anisotropy vanishes, is found to be approximately 120 K, which is 10 K lower than the bulk value. The Verwey transition is close to 110 K, again about 10 K lower than the bulk crystal value. Below the Verwey transition temperature, the uniaxial anisotropy of the monoclinic phase increases gradually and asymptotically approaches a constant value indicating a smooth structural transition rather than a sudden change. Resonance linewidth and effective damping increases abruptly below 110 K. The effective damping constant is determined to be ~ 0.01 and is independent of temperature from 300 K to 120 K .

3.2 Introduction

Complete characterization of a material is generally required before it can be used for any practical application. It is well known that magnetic properties of magnetite films differ from their bulk value due to substrate-induced effects like strain, stoichiometry, defect states, etc. This emphasizes the importance of choosing the appropriate substrate for a particular application. There are several reports in existing literature that study the Verwey phase transition of magnetite film grown on various substrates (GaAs, MgO, $MgAl_2O_4$ and $SrTiO_3$)[1] with the same symmetry as magnetite but with different crystal structures. Despite several FMR studies available in literature [2, 3], broadband characterization of magnetite is still lacking, despite it providing a more accurate estimate of dynamic properties like the gyromagnetic ratio and the damping constant. FMR analysis using X-band frequency can lead to less accurate results because the measurement covers lower fields, where the sample may not be fully saturated. Another advantage of broadband FMR for this particular study is that below the Verwey transition the analysis is done for the external field applied along the *c* axis of the monoclinic phase. This prevents a field induced change of the *c* axis during the measurements [4], which is a possibility for torque magnetometry. Recently we have reported structural and magnetic properties of magnetite films epitaxially grown on isostructural $MgGa_2O_4$ substrate which exhibit improved structural and magnetic quality compared to films grown on other substrates [5]. As continued characterization, we have performed broadband FMR characterization of this film from 300 K to 75 K to investigate the temperature dependence of the magnetic anisotropy and magnetization dynamics. Comparing the results obtained from this study with information available in the literature indicates that the Verwey transition temperature in magnetite films depends on substrate and stoichiometry of the film.

3.3 Experimental details

Temperature-dependent ferromagnetic resonance (FMR) is studied on magnetite (Fe_3O_4) thin film of thickness 30 nm, grown on isostructural $MgGa_2O_4$ (001) substrate using pulsed laser deposition method (details of deposition and characterization are provided in reference [5]). These films have a lattice mismatch of -1.4% with the substrate and are single crystalline, epitaxially grown as evident from XRD results. Our FMR measurement system is a custom designed broadband ferromagnetic resonance setup utilizing a coplanar waveguide (CPW) for the microwave excitation of the sample and operates over a frequency range from 1-40 GHz [6]. The system is housed in a Lakeshore cryostat (10-300 K). FMR measurements are done at a fixed frequency by sweeping the external magnetic field through resonance. The transmitted power is detected using a Schottky diode with a lock-in technique by adding a small modulation field to the external magnetic field. The FMR is performed on the sample with the external magnetic field applied within the plane of the film along [010] (in-plane hard axis), and [110] (in-plane easy axis) directions of the cubic phase.

3.4 Interpretation of FMR data

It is well known that magnetite undergoes a structural phase transition at approximately 120 K known as the Verwey transition [7]. Above the transition temperature the crystal structure is cubic with a four-fold anisotropy. Below the transition, it has a monoclinic structure with the original cubic $\langle 100 \rangle$ direction as c axis (which becomes magnetic easy axis of the monoclinic phase) while the original cubic $\langle 110 \rangle$ direction, become the a and b axis of the mocnoclinic phase. More precisely, the monoclinic c axis is expected to be 0.23° tilted away from original cubic $\langle 100 \rangle$ axis towards [111] direction [8, 9]. In absence of an external field during cool down through the Verwey transition, the c axis of monoclinic phase will be distributed equally along three equivalent $\langle 100 \rangle$ axes, and a and b axes will be distributed among six equivalent $\langle 110 \rangle$ axes [10]. Therefore we applied an external field of 1.4 T along the cubic [010] direction during cool down through

the Verwey transition, which will fix the *c* axis of the whole crystal in the direction of the applied magnetic field and the face diagonals of the original cubic phase, perpendicular to *c* axis become the *a* and *b* axis of the monoclinic phase (figure 3.1). However, twinning of the *a* and *b* axis cannot be removed by this method. This gives rise to an in-plane uniaxial anisotropy with the *c* axis as the easy axis.

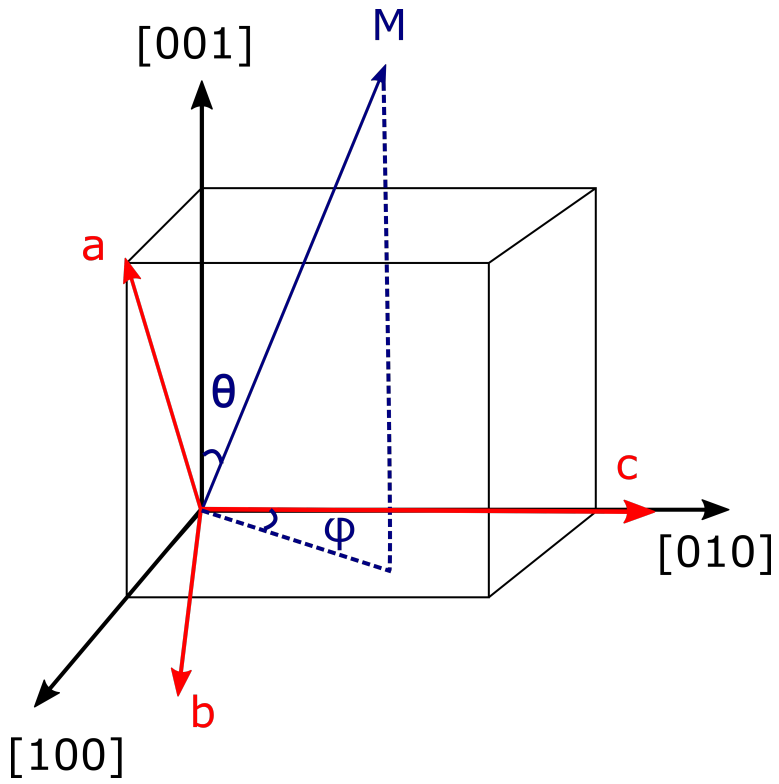

Figure 3.1: Coordinate system for the sample with respect to cube axis. [001] is normal to the film plane. [010] is the monoclinic *c* axis and *a* and *b* are the axes of monoclinic phase, in the plane containing [001] and [100] direction.

Above the Verwey transition (when the film has cubic symmetry), broadband FMR (10-40 GHz) measurements were done with the external field applied in the film plane, along the [010] direction (in-plane hard axis), and [110] direction (in-plane easy axis) of the cubic phase, as shown in figure 3.2. The combined data set is fitted using the Kittel equation 3.1 and 3.2 [11].

$$f_{hard} = \gamma' \sqrt{[H_{res,hard} + H_4] \cdot [H_{res,hard} + 4\pi M_{eff} + H_4]} \tag{3.1}$$

$$f_{easy} = \gamma' \sqrt{[H_{res,easy} - H_4] \cdot [H_{res,easy} + 4\pi M_{eff} + \frac{1}{2} H_4]} \tag{3.2}$$

Where f is the microwave frequency, and the shared fit parameters are $\gamma' = \frac{\gamma}{2\pi}$ is reduced gyromagnetic ratio, H_{res} is the resonance field, H_4 the in-plane four-fold anisotropy field and M_{eff} the effective magnetization, which includes the demagnetization field $4\pi M_s$ and the perpendicular anisotropy $K_u^{\perp}$:

$$4\pi M_{eff} = 4\pi M_s + \frac{2K_u^{\perp}}{M_s} \tag{3.3}$$

where M_s is the saturation magnetization and $K_u^{\perp}$ is the perpendicular anisotropy constant.

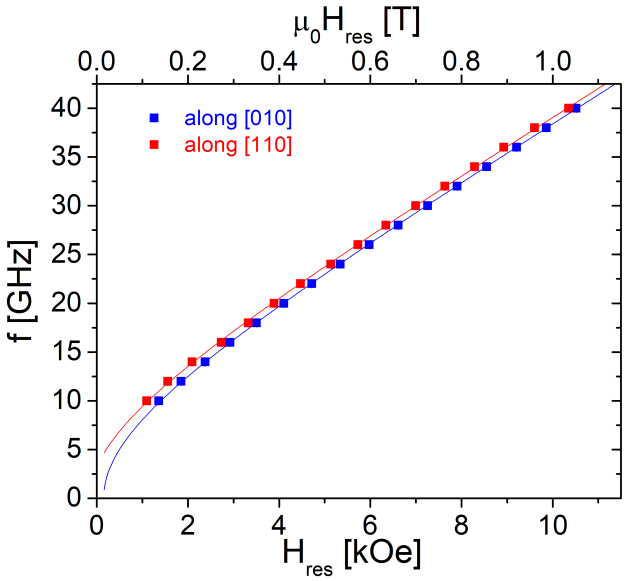

Figure 3.2: Frequency dependence of FMR resonance field along the [010] direction (blue symbols, in-plane hard axis) and [110] direction (red symbols, in-plane easy axis) at 300 K for a 30 nm thick Fe_3O_4 film grown on $MgGa_2O_4$ (001). Solid lines are a fit to the Kittel equations (1) and (2) with shared fitting parameters.

A monoclinic phase is stabilized below the the Verwey transition. For a monoclinic system with in-plane uniaxial anisotropy, the dispersion relation can be written as equation 3.4 [12]. A detailed description is discussed in the appendix.

$$f = \gamma' \sqrt{[H_{res} + 2H_u^{||} + 4\pi M_{eff}] \cdot [H_{res} + H_u^{||}]} \tag{3.4}$$

3.5 Results

In-plane broadband FMR measurements were carried out along [010] and [110] direction at different temperatures. Data at 300 K is shown in figure 3.2, in addition we have carried out measurements of the resonance field vs temperature at 30 GHz, as shown in figure 3.3. FMR spectrum at 30 GHz for measurements carried out at different temperatures along [010] direction is shown in appendix (figure 3.8). The difference in resonance field along [010] (in-plane hard axis) and [110] (in-plane easy axis) starts to decrease below 200 K, this difference for the film in our study becomes zero near 120 K indicating a vanishing in-plane anisotropy known as isotropic point. When the external magnetic field is applied along the [110] direction the shift in resonance field below the Verwey transition should not be interpreted in terms of magnetocrystalline anisotropy because in this configuration a unique c axis is not defined. Instead one expects a mixture of magnetic axes in the sample and hence the data is only shown for completeness. For the film in our study the isotropic point is about 10 K lower than the temperature observed in bulk single crystals [13]. As the temperature is lowered there is a sudden drop in resonance field at about 110 K, which is close to the Verwey transition temperature of the Fe_3O_4 film as determined from the resistivity measurement on the same sample which showed that the Verwey transition is at about 111 K [5]. The lowering of the transition temperature compared to the bulk value can be due to both non-stoichiometry and stress in the film [14–16]. The saturation magnetization of the monoclinic phase (low temperature phase) is known to be only ~ 0.1 % smaller than that of the cubic phase (above T_v) [9] which means that any change in M_{eff} would be indicative of a change of the perpendicular anisotropy.

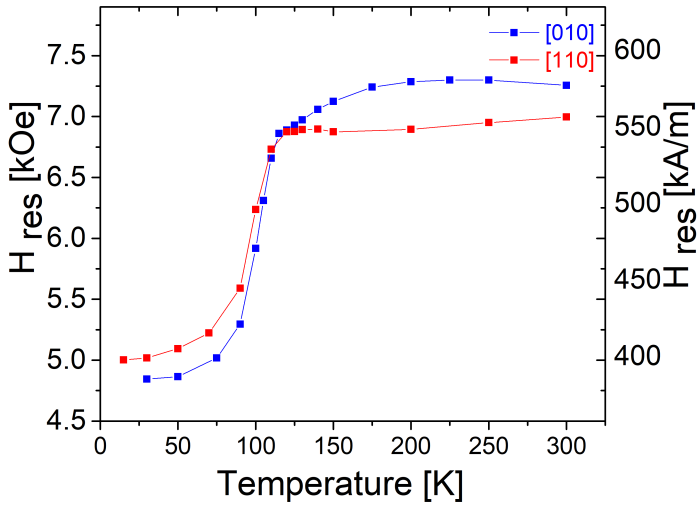

Figure 3.3: Resonance field vs Temperature at 30 GHz for external magnetic field applied along [010] direction (blue symbols) and [110] direction (red symbols). Solid lines are guide to the eye.

For the FMR measurements of the cubic phase (300 K-120 K), the combined in-plane broadband FMR data sets were fit using the Kittel equations (3.1) and (3.2). This yields the magnetocrystalline anisotropy field, H_4 (or anisotropy constant $K_1 = \frac{1}{2}M_s H_4$), effective magnetization, M_{eff}, and reduced gyromagnetic ratio, γ', as shown in figure 3.4. Below the Verwey transition temperature (110 K), the film becomes monoclinic with a unique c axis along [010] direction due to the presence of an external magnetic field of 1.4 T along this axis during cooling [4]. At each temperature the frequency dependence of the resonance field is measured along the [010] direction and fitted using equation (3.4). Due to the large error margins of the resonance field, H_{res} caused by the increased linewidth in this temperature range it was necessary to fix the gyromagnetic ratio to $\gamma' = 2.93$ GHz/kOe, which is the value obtained at a temperature 120 K. While we also measured FMR data along the orignal cubic [110] direction, this data is not used in determining the anisotropy field below the Verwey transition temperature as in this case no unique c axis is defined complicating the data analysis.

The effective magnetization, which is sum of demagnetization field and perpendicular anisotropy field (equation 3.3), does not show much variation from 300 K to 120 K, suggesting that there is

no change in perpendicular anisotropy in the film, assuming constant saturation magnetization in this temperature range (saturation magnetization only vary $\sim$ 5% in the range 300 K to 4 K[17]). At the Verwey transition temperature, 110 K, M_{eff} is increased by about 60 emu/cc (figure 3.4 (a), suggesting that there is a change in the perpendicular anisotropy in the monoclinic phase. The large error margin below the transition is due to the large increase in linewidth of the FMR signal which adds to the error in resonance field. There is no significant variation in gyromagnetic ratio from room temperature to 110 K (figure 3.4 (b)). Figure 3.4 (c) is the plot of the magnetocrystalline anisotropy, calculated from the in-plane anisotropy field, H_4, using the relation $H_4 = \frac{2K_1}{M_s}$ where M_s is the saturation magnetization, which is kept constant at 466 emu/cc measured at 300 K. The magnetocrystalline anisotropy has the value of -3.5 kJ/m^3 at room temperature which is about one third of the bulk crystal value of -11 kJ/m^3 [18]. The anisotropy constant K_1 has a maximum at about 200 K, and reduces to zero at 120 K. A similar trend in K_1 is also observed by other authors in earlier reports for bulk and thin magnetite films [2, 14].

Figure 3.5 shows the uniaxial anisotropy field as the temperature decreases below the Verwey transition temperature. The uniaxial anisotropy field increases gradually as the temperature decreases and approaches a constant value below 75 K, indicating that there is a continuous change in the magnetocrystalline anisotropy. Because the magnetocrystalline anisotropy is linked to the crystal structure, this implies that there is a gradual change of the crystal structure from cubic to monoclinic. The value of H_u obtained at 75 K is 1268 ± 341 Oe, is of the same order of magnitude ($\sim$ 1500 Oe at 50 K) as found by Heijden et al for the magnetite film grown on MgO [2].

Figure 3.6 shows the temperature dependence of the linewidth at 30 GHz for an applied field along the [010] (figure 3.6 (a)) and [110] direction (figure 3.6 (b)). The linewidth measured along the [010] direction increases sharply below 120 K. However, along the [110] direction there is a minimum of the linewidth near 120 K, and below 90 K, the linewidth starts decreasing again. While the exact reason for this reduction of the linewidth below 90 K is not known, this could be due to partial removal of twinning. Removal of twinning was observed in the temperature range of 80-90 K when the applied field is parallel to cube face diagonal (the [110] direction) as men-

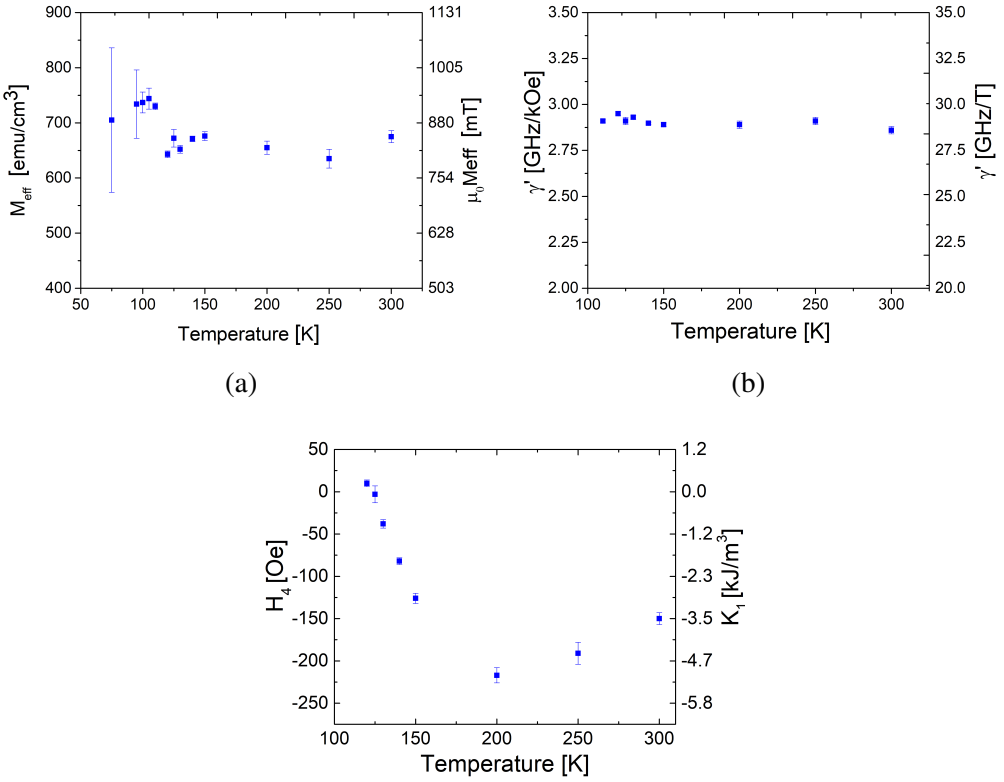

Figure 3.4: Temperature dependence of parameters extracted from Kittel fit, (a) effective magnetization, (b) reduced gyromagnetic ratio γ', and (c) cubic magnetocrystalline anisotropy.

tioned by Bonstrom [19]. It is to be noted that, for measurements along cubic [110] direction, no external field is applied between the individual measurements when the sample was cooled down. However, the field applied during the measurements is of the order of 5-7 kOe (see figure 3.3) and hence can cause the removal of twinning in subsequent measurements of lower temperatures. The sudden increase in linewidth indicates that magnetic inhomogeneities increase below 120 K which is the isotropic point of the sample. There is also an increase in the effective damping α_{eff} of the film below 120 K as can be seen in figure 3.7 (b). The effective damping was extracted by fitting the linewidth vs frequency data along [010] direction with the equation 3.5. The fitting is done down to 100 K, below which the linewidth became too large and the frequency dependence is no longer linear because of scatter in the data. Figure 3.7 (b) shows that the effective damping value is ~ 0.01 in the range 120-300 K, which is lower than the damping constant quoted by

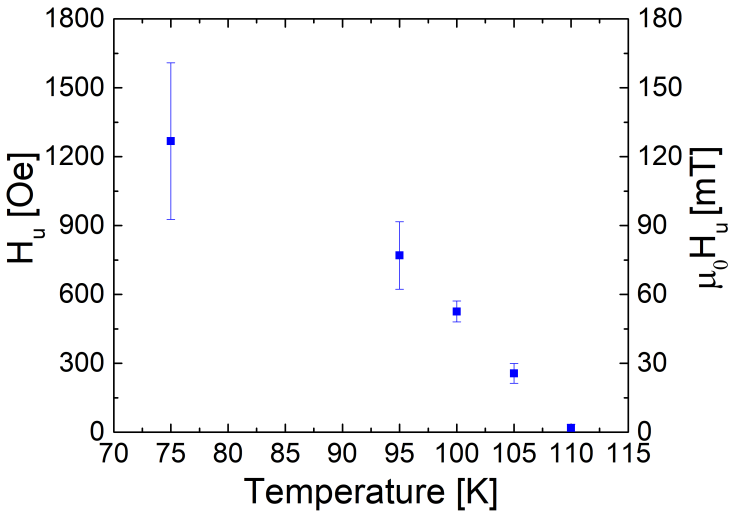

Figure 3.5: The temperature dependence of the in-plane uniaxial anisotropy below 120 K.

others, 0.037 by Guisan [20] and 0.02 by Nagata [21].

$$\Delta H = \Delta H_0 + \frac{2}{\sqrt{3}} \cdot \alpha_{eff} \cdot \frac{f}{\gamma'} \tag{3.5}$$

Here f is the microwave frequency, α_{eff} is the effective Gilbert damping parameter, ΔH is the peak-to-peak linewidth, ΔH_0 is the linewidth extrapolated to zero frequency and γ' is the reduced gyromagnetic ratio.

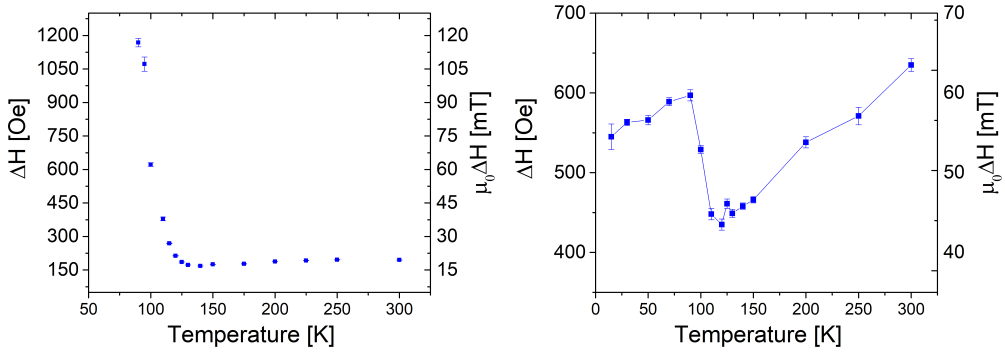

(a) (b)

Figure 3.6: The temperature dependence of linewidth at f=30 GHz when the applied field is parallel to (a) [010] and (b) [110] direction.

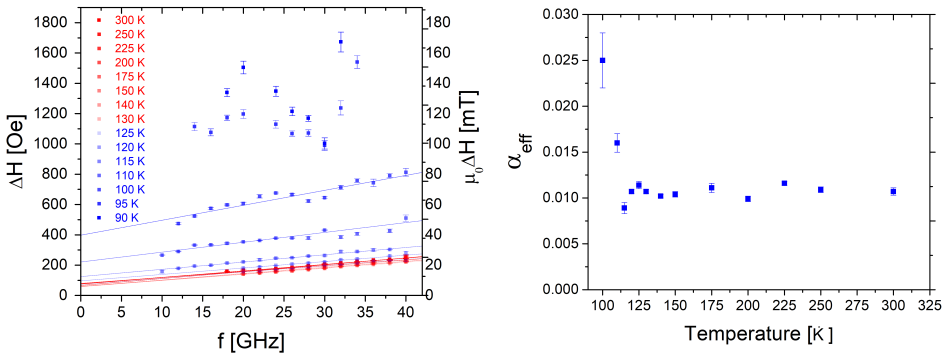

(a) (b)

Figure 3.7: (a) Linewidth dependence on the frequency for the external field in cubic [010] direction at different temperatures. Solid line is the fit to the equation 3.5. (b) The effective damping vs. temperature.

3.6 Conclusion

In summary, we have investigated the Verwey transition in a magnetite thin film grown on isostructural substrate ($MgGa_2O_4$) by broadband FMR analysis, which indicates, despite having improved structural quality, the Verwey transition temperature $(\sim 110K)$ is significantly lower than the bulk value $(\sim 120K)$. This suggests that the substrate induced strain in the film strongly affects the Verwey transition temperature. The magnetocrystalline anisotropy is also effected by strain. The in-plane uniaxial anisotropy below the Verwey transition evolves gradually, suggesting that cubic-monoclinic phase transition occurs continuously over a wide temperature range.

3.7 Acknowledgements

A. Srivastava would like to acknowledge support by NASA Grant NASA CAN80NSSC18M0023 and A. Singh acknowledges the supported by the National Science Foundation (NSF) Grant No. ECCS-1509875. C. K. Mewes acknowledges the support by NSF CAREER Award No. 1452670.

3.8 Appendix

In the monoclinic phase, below the Verwey transition, the magnetocrystalline energy can be expressed by equation 3.6 [3, 17].

$$E_a = K_a\alpha_a^2 + K_b\alpha_b^2 + K_{aa}\alpha_a^4 + K_{bb}\alpha_b^4 + K_{ab}\alpha_a^2\alpha_b^2 - K_u\alpha_{111}^2 \tag{3.6}$$

where α_a, α_b and α_{111} are direction cosines of magnetization with respect to monoclinic a,b, and cubic [111] axes. The last term comes from the uniaxial anisotropy resulting from monoclinic distortion of the unit cell relative to the cubic phase. In case of unstrained sample, elongation in [111] and $[11\bar{1}]$ direction is allowed, thus the energy can be expressed as equation 3.7 [9, 22].

$$E_a = \tilde{K}_a\alpha_a^2 + \tilde{K}_b\alpha_b^2 + K_{aa}\alpha_a^4 + K_{bb}\alpha_b^4 + K_{ab}\alpha_a^2\alpha_b^2 \tag{3.7}$$

with $\tilde{K_a} \equiv K_a - \frac{1}{3}K_u, \tilde{K_b} \equiv K_b + \frac{1}{3}K_u$ [17].

Neglecting higher order terms,

$$E_a = \tilde{K}_a\alpha_a^2 + \tilde{K}_b\alpha_b^2 \tag{3.8}$$

Considering the twinning of a and b axes, the in-plane uniaxial anisotropy is given by $K_u^{||} = -\frac{1}{2}(\tilde{K_a} + \tilde{K_b})$ and the effective uniaxial out of plane anisotropy as $K_u^{*\perp} = K_u^{\perp} - \frac{1}{2}(\tilde{K_a} + \tilde{K_b})$ [2]. The dispersion relation for a monoclinic crystal with in-plane uniaxial anisotropy can be written as equation 3.9 [12]

$$f = \gamma'\sqrt{\left[H_{res} + H_u^{||}\cos^2(\phi_H) + 4\pi M_{eff}^*\right] \cdot \left[H_{res} + H_u^{||}\cos(2\phi_H)\right]} \tag{3.9}$$

For $\phi_H = 0^\circ$ above equation can be written as

$$f = \gamma'\sqrt{[H_{res} + H_u^{||} + 4\pi M_{eff}^*] \cdot [H_{res} + H_u^{||}]} \tag{3.10}$$

where f is the microwave frequency, γ' is reduced gyromagnetic ratio, H_{res} is the resonance field,

$H_u^{||} = \frac{2K_u^{||}}{M_s}$ is the in-plane uniaxial anisotropy field and M_{eff}^* is the effective magnetization given by [2]

$$4\pi M_{eff}^* = 4\pi M_s + \frac{2K_u^{*\perp}}{M_s} = 4\pi M_s + \frac{2K_u^{\perp}}{M_s} - \frac{\tilde{K}_a + \tilde{K}_b}{M_s} = 4\pi M_{eff} + H_u^{||}$$

Using above expression in equation 3.10, the dispersion relation becomes

$$f = \gamma' \sqrt{[H_{res} + 2H_u^{||} + 4\pi M_{eff}] \cdot [H_{res} + H_u^{||}]} \tag{3.11}$$

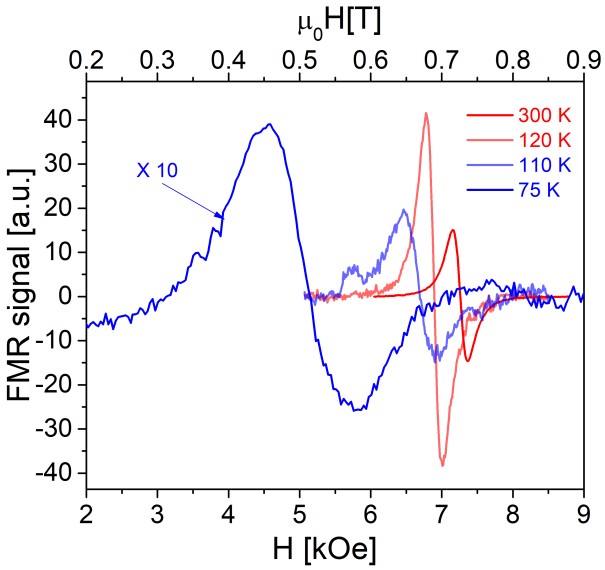

Figure 3.8: FMR spectra at different temperatures at 30 GHz, for the external field along [010] direction. The spectra at 75 K is amplified 10 times for comparison.

3.9 References

[1] S. Kale, S. Bhagat, S. Lofland, T. Scabarozi, S. Ogale, A. Orozco, S. Shinde, T. Venkatesan, B. Hannoyer, B. Mercey, *et al.*, *Film thickness and temperature dependence of the magnetic properties of pulsed-laser-deposited Fe_3O_4 films on different substrates*, Physical Review B **64**, 205413 (2001).

[2] P. Van der Heijden, M. Van Opstal, C. Swüste, P. Bloemen, J. Gaines, and W. De Jonge, *A ferromagnetic resonance study on ultra-thin Fe_3O_4 layers grown on (001) MgO*, Journal of Magnetism and Magnetic Materials **182**, 71 (1998).

[3] B. Aktas, *FMR properties of epitaxial Fe_3O_4 films on MgO (100)*, Thin Solid Films **307**, 250 (1997).

[4] B. Calhoun, *Magnetic and electric properties of magnetite at low temperatures*, Physical Review **94**, 1577 (1954).

[5] A. V. Singh, A. Srivastava, J. B. Mohammadi, S. Regmi, U. Bhat, R. Datta, T. Mewes, and A. Gupta, *Studies of electrical and magnetic properties across the Verwey transition in epitaxial magnetite thin films*, Journal of Applied Physics **126**, 093902 (2019).

[6] S. Keshavarz, Y. Xu, S. Hrdy, C. Lemley, T. Mewes, and Y. Bao, *Relaxation of Polymer Coated Fe_3O_4 Magnetic Nanoparticles in Aqueous Solution*, IEEE Transactions on Magnetics **46**, 1541 (2010).

[7] E. Verwey, *Electronic conduction of magnetite (Fe_3O_4) and its transition point at low temperatures*, Nature **144**, 327 (1939).

[8] M. Iizumi, T. Koetzle, G. Shirane, S. Chikazumi, M. Matsui, and S. Todo, *Structure of magnetite (Fe_3O_4) below the Verwey transition temperature*, Acta Crystallographica Section B: Structural Crystallography and Crystal Chemistry **38**, 2121 (1982).

[9] M. Matsui, S. Tōdō, and S. Chikazumi, *Magnetization of low temperature phase of Fe_3O_4*, Journal of the Physical Society of Japan **43**, 47 (1977).

[10] W. Palmer, *Magnetocrystalline anisotropy of magnetite at low temperature*, Physical Review **131**, 1057 (1963).

[11] C. Pang, A. Srivastava, M. M. Lockart, T. Mewes, M. K. Bowman, N. Bao, L. Shen, and A. Gupta, *Magnetic properties of semiconducting spinel $CdCr_2S_4$ nanostructured films grown by low-pressure metal organic chemical vapor deposition*, ACS Applied Electronic Materials (2019).

[12] J. B. Mohammadi, J. M. Jones, S. Paul, B. Khodadadi, C. K. Mewes, T. Mewes, and C. Kaiser, *Broadband ferromagnetic resonance characterization of anisotropies and relaxation in exchange-biased IrMn/CoFe bilayers*, Physical Review B **95**, 064414 (2017).

[13] Z. Kakol and J. Honig, *Influence of deviations from ideal stoichiometry on the anisotropy parameters of magnetite $Fe_{3(1-\delta)}O_4$*, Physical Review B **40**, 9090 (1989).

[14] R. Aragón, *Cubic magnetic anisotropy of nonstoichiometric magnetite*, Physical Review B **46**, 5334 (1992).

[15] Y. Kakudate, N. Mori, and Y. Kino, *Pressure effect on the anomalous electrical conductivity of magnetite*, Journal of Magnetism and Magnetic Materials **12**, 22 (1979).

[16] S. Tamura, *Pressure dependence of the Verwey temperature of $Fe_{3-y}O_4$ obtained by magnetic permeability measurements*, Journal of the Physical Society of Japan **59**, 4462 (1990).

[17] K. Abe, Y. Miyamoto, and S. Chikazumi, *Magnetocrystalline anisotropy of low temperature phase of magnetite*, Journal of the Physical Society of Japan **41**, 1894 (1976).

[18] L. Bickford Jr, *Ferromagnetic resonance absorption in magnetite single crystals*, Physical Review **78**, 449 (1950).

[19] D. Bonstrom, A. Morrish, and L. Watt, *Magnetic properties of the low-temperature form of magnetite*, Journal of Applied Physics **32**, S272 (1961).

[20] S. Serrano-Guisan, H.-C. Wu, C. Boothman, M. Abid, B. Chun, I. Shvets, and H. Schumacher, *Thickness dependence of the effective damping in epitaxial Fe_3O_4/MgO thin films*, Journal of Applied Physics **109**, 013907 (2011).

[21] M. Nagata, K. Tanabe, T. Moriyama, D. Chiba, J.-I. Ohe, M. Myoka, T. Niizeki, H. Yanagihara, E. Kita, and T. Ono, *Ferromagnetic resonance in magnetite thin films*, IEEE Transactions on Magnetics **50**, 1 (2013).

[22] Z. Kakol, R. Pribble, and J. Honig, *Magnetocrystalline anisotropy of $Fe_{3(1-\delta)}O_4, 0 \leq \delta <$ 0.01*, Solid State Communications **69**, 793 (1989).

CHAPTER 4

MAGNETIC PROPERTIES OF SEMICONDUCTING SPINEL $CdCr_2S_4$ FILMS GROWN BY LOW-PRESSURE METAL ORGANIC CHEMICAL VAPOR DEPOSITION

Chao Pang[1,2], Abhishek Srivastava[1,3], Molly Lockart[4], Tim Mewes[1,3], Michael K. Bowman[4], Ningzhong Bao[2], Liming Shen[2], and Arunava Gupta[1]

1: Center for Materials for Information Technology (MINT), The University of Alabama, Tuscaloosa, AL 35487, United States.

2: State Key Laboratory of Materials-Oriented Chemical Engineering, Nanjing Tech University, Nanjing, Jiangsu 210009, P. R. China.

3: Department of Physics and Astronomy, The University of Alabama, Tuscaloosa, AL 35487, United States.

4: Department of Chemistry and Biochemistry, The University of Alabama, Tuscaloosa, AL 35487, United States.

4.1 Abstract

Magnetic semiconductors are being extensively investigated because of their promise to provide new functionalities and device concepts for spintronic applications. Nevertheless, it remains a challenge to obtain high-quality thin films of these materials for device usage, particularly of chalcogenide-based semiconductors. The chalcogenide spinel $CdCr_2S_4$ is a well-established ferromagnetic semiconductor. In bulk form, it exhibits unique properties such as colossal magnetocapacitance and magnetoresistance effects and is a promising candidate for spintronic applications. Because of its semiconducting properties and band gap in the visible wavelength range, $CdCr_2S_4$ offers exciting possibilities for tailoring its optical and magnetic properties. However,

applications that utilize its unique combination of optical, electrical, and magnetic properties are limited because of difficulties in growing high-quality films. Herein, we demonstrate a simple low-pressure metal organic chemical vapor deposition (MOCVD) method for growth of high-quality $CdCr_2S_4$ thin films using metal organic precursors of Cd and Cr, which provides an attractive route for scaling to large areas. The deposited films are uniform with excellent phase purity, morphology, and crystallinity. In addition to structural and optical characterization, the static and dynamic magnetic properties of the MOCVD grown films have been investigated in detail.

4.2 Introduction

Over the past few decades, compounds combining semiconducting and ferromagnetic properties have emerged as an important field of materials science [1–5]. Magnetic semiconductors hold a very special position in the field of spintronics because they can potentially enable effective manipulation of both charge and spin. This feature is especially important in devices combining logic functions and information storage capability [6–9]. Most investigations thus far have focused on doping magnetic elements to obtain magnetic semiconductors or dilute magnetic oxides [10–12]. However, the development and understanding of novel magnetic materials that are intrinsically semiconducting remains one of the most challenging research topic in materials science [13–15]. The remarkable chromium-based chalcogenide spinels (chalcospinels), ACr_2X_4 (A = Cu, Cd, Hg, Fe, Co, etc.; X = S, Se, Te), with diverse electronic properties, offer new opportunities to investigate the origin and control of ferromagnetism in magnetic semiconductors. The chalcospinels exhibit unusual magnetic properties resulting from exchange and superexchange interactions between Cr^{3+} ions with half-filled t_{2g} ground states (S = 3/2) and no charge or orbital degrees of freedom [16, 17]. Moreover, depending on the the nature of A-site cation(s), they display metallic, semiconducting, or insulating characteristics resulting from combined strong electronic correlation and strong coupling of structural and electronic degrees of freedom [16, 18]. Among chalcospinels, only a few of the known single-phase materials are both ferromagnetic and semiconducting. They exhibit unique and unusual physicochemical properties such as half-

metallicity and dissipationless anomalous Hall current [19–22]. The prototypical chalcospinel ferromagnetic semiconductor, $CdCr_2S_4$, has been widely studied in the bulk because of its unique properties such as colossal magnetoresistance, magnetic field-induced structural transformation, spin and orbital frustration, and relaxor ferroelectricity combined with colossal magnetocapacitive coupling [23–26]. The colossal magnetocapacitance and magnetoresistance effects makes it an interesting candidate for spintronic applications and a potential multiferroic material [27]. $CdCr_2S_4$ offers the exciting possibility of tailoring its optical and magnetic properties because of its semiconducting characteristics and its band gap in the visible wavelength range [28]. However, applications of $CdCr_2S_4$ that utilize its unique combination of optical, electrical, and ferromagnetic properties are limited.

We have previously reported on the chemical syntheses of different chalcospinel nanocrystals with various shapes and sizes [29–32]. However, none of these magnetic chalcospinel nanocrystals are semiconductors. We recently succeeded in synthesizing magnetic semiconducting $CdCr_2S_4$ nanocrystals using a novel "seed-mediated" growth method [33]. Advancing on this work, we have explored chemical synthetic routes to obtain high-quality nanostructured $CdCr_2S_4$ thin film for potential device applications. Thus far, synthetic routes for chalcospinel films mainly include a wet chemistry method and a multiple-step spin-coating method using nanocrystals [33]. The reported wet chemistry methods for the growth of $CdCr_2S_4$ films, such as chemical bath deposition and electrochemical deposition, result in the poor crystallinity and impurities [34–37]. For multiple-step spin-coating method, the nanocrystal defects and capped organic ligands negatively influence the electrical properties of the films, and additional annealing results in inevitable grain boundary defects and sulfur deficiency [38]. Precursors reported in the literature for the chemical synthesis of bulk $CdCr_2S_4$, including elemental Cd/Cr, CdS, Cr_2S_3, $CdCl_2$, $CrCl_3$, CdO, CrO_3, and $CdCr_2S_4$, require elevated temperature for volatilization and reaction [33, 39, 40]. Thus, development of suitable Cadmium and Chromium precursors with sufficient volatility and stability for the growth of high-quality nanostructured $CdCr_2S_4$ films by chemical methods is an important challenge and a bottleneck for development of chalcogenide-based spintronic/electronic de-

vices.

Herein, we report a simple and efficient low-pressure metal-organic chemical vapor deposition (MOCVD) method for the growth of high-quality ferromagnetic semiconducting $CdCr_2S_4$ nanostructured films. MOCVD is a desirable film deposition technique for conformal growth of high-quality films with excellent uniformity over large areas. It is widely utilized in the electronics industry for deposition of a variety of semiconducting and oxide films [41, 42]. Low-pressure MOCVD often enables film growth at lower temperatures than is possible at atmospheric pressure and with better coverage and homogeneity. In this work, we have explored the use of transition metal alkyldithiocarbamate complexes that have previously been employed as single-source precursors to deposit II/VI compound semiconductor films [43, 44]. The dithiocarbamate complexes are generally air-stable with reasonable volatility and can provide clean deposition with minimum carbon incorporation. We have developed a gram-scale chemical synthesis method for obtaining high-purity diethyldithiocarbamate complexes of Cadmium(II) and Chromium(III) $(Cd(S_2CNEt_2)_2 and Cr(S_2CNEt_2)_3))$. A homogeneous mixture of these precursors is used in the presence of sulfur vapor for low pressure MOCVD growth of nanostructured $CdCr_2S_4$ films on borosilicate glass substrates. The deposited films are uniform with excellent phase purity, morphology, and crystallinity, which have grain sizes from 100 to 200 nm. Besides determining the band gap from optical absorption measurements, we have studied in detail the static and dynamic magnetic properties of the $CdCr_2S_4$ films.

4.3 Experimental section

Chemicals. All chemicals were used as received. Sodium diethyldithiocarbamate trihydrate $(NaS_2CN(C_2H_5)_2 \cdot 3H_2O$, ACS reagent) was purchased from Chem-Impex International. Isopropyl alcohol (IPA, $\geq 98.0\%$), dichloromethane $(CH_2Cl_2, ACSreagent)$, sulfur powder (S, 99.5%), chromium chloride hexahydrate $(CrCl_3 \cdot 6H_2O, 98\%)$, and cadmium chloride $(CdCl_2, 99\%)$ were obtained from Alfa Aesar.

Synthesis and Purification of $Cr(S_2CNEt_2)_3$. In a typical reaction, $NaS_2CN(C_2H_5)_2 \cdot 3H_2O$

(2.253 g, 10 mmol) was dissolved in 30 mL of IPA, and the solution was sonicated for 20 min. At the same time, $CrCl_3 \cdot 6H_2O$ (0.89 g, 3.4 mmol) was dissolved in 20 mL of IPA and magnetically stirred for 20 min at 70 °C. The sodium diethyldithiocarbamate solution then was added to the $CrCl_3 \cdot 6H_2O$ solution with stirring at 90 °C and refluxed for 5 h. After reaction, a blue-green solid was collected by centrifugation and dissolved in dichloromethane. The $Cr(S_2CNEt_2)_3$ solution and insoluble white impurities were separated by centrifugation at 8000 rpm for 6 min. The resulting solution was transferred to a beaker with 400 mL of IPA added. After recrystallization for 3 h, the dark blue precipitate was isolated via centrifugation at 6500 rpm for 5 min and washed once before drying.

Synthesis and Purification of $Cd(S_2CNEt_2)_2$. In a typical reaction, $NaS_2CN(C_2H_5)_2 \cdot 3H_2O$ (2.253 g, 10 mmol) was dissolved in 30 mL of IPA, and the solution was sonicated for 20 min. At the same time, $CdCl_2$ (0.92 g, 5 mmol) was dissolved in 20 mL of deionized water and magnetically stirred for 20 min. The $CdCl_2$ solution was added to sodium diethyldithiocarbamate solution with stirring at room temperature for 1 h. The resulting white precipitate was collected by centrifugation at 6500 rpm for 5 min and washed three times by using IPA before drying.

Deposition of $CdCr_2S_4$ Films. Borosilicate glass substrates (0.5 cm × 0.5 cm, VWR International) were cleaned by using detergent followed by repeated washing with deionized water prior to ultrasonic cleaning in acetone and isopropanol, each for 30 min. The low-pressure MOCVD system consists of a quartz tube reactor with a nominal diameter of 1.5 in. and length of 30 in., housed in a tubular furnace. The pressure inside the quartz tube was maintained at $\sim$ 0.2 Torr by using a roughing pump. The sulfur powder and mixture of the synthesized $Cd(S_2CNEt_2)_2$ and $Cr(S_2CNEt_2)_3$ powders were placed upstream in separate porcelain boats in lower temperature zones of the tubular furnace. After pumping for 10 min, the sulfur powder was heated to 180 °C, while the mixture of $Cd(S_2CNEt_2)_2$ and $Cr(S_2CNEt_2)_3$ powder was simultaneously heated to 400 °C. Ultrahigh-purity argon gas, the flow rate of which was maintained at 300 sccm by using a Brooks Instrument Quantum gas mass flow controller (MFC), was used as a carrier gas for the sublimed precursors to be transported to the reaction zone, where it decomposed on the glass

substrates (500 °C) to form polycrystalline $CdCr_2S_4$ thin films. After deposition for 60 min, the furnace was cooled, and the $CdCr_2S_4$ thin films were taken out for characterization.

Structural and Magnetic Characterization. XRD patterns were recorded on a Bruker D8 X-ray diffractometer equipped with a Cu K_α radiation source. Scanning electron microscopy (SEM) analysis was performed using a JEOL 7000 FESEM equipped with EDX detector. Surface roughness was determined by atomic force microscopy (AFM, Asylum Research). The absorption characteristics of the films were recorded with a UV-vis spectrophotometer (Agilent, Cary 500, USA). Band gap data processing was done using OriginPro 2018b and MATLAB R2018b software. X-ray photoelectron spectroscopy (XPS) analysis was performed on a Thermo Scientific K-Alpha spectrometer. Magnetic measurements were performed using a Quantum Design Dynacool Physical Properties Measurement System (PPMS) equipped with a Vibrating Sample Magnetometer (VSM). Continuous wave (CW) EPR spectra were recorded in the temperature range 20-290 K on an ELEXSYS E680 EPR spectrometer with a Flexline ER 4118 CF cryostat and an ER 4118X-MD4 ENDOR resonator (Bruker-Biospin, Billerica, MA). CW EPR measurements were performed at a nominal microwave frequency of 9.75 GHz with a microwave power of 0.02 mW, a modulation frequency of 100 kHz, and a modulation amplitude of 5.0 G. Measurements were made to check for power saturation at various temperatures. CW data processing was done with Bruker's Xepr software (Bruker-Biospin, Billerica, MA) and Origin (OriginPro, 2018b). We evaluated the double integrals (DI) by subtracting the baseline and double integrating the CW spectrum over a window that encompassed the full first-derivative peak and sufficient baseline on either side of the peak. The DI could not be calculated for temperatures below 55 K for the in-plane measurements and 65 K for the out-of-plane measurements because the first-derivative peaks were too broad and extended past the maximum magnetic field sweep width. EPR linewidths were calculated as the peak-to-peak linewidth. The ferromagnetic resonance properties were measured by using a custom-designed broadband ferromagnetic resonance setup using coplanar waveguide for microwave transmission from the microwave source and operating in the 1-40 GHz range. The external magnetic field was swept through the resonance field of

the sample at a fixed frequency. The transmitted power through the sample was detected by a rf diode. The lock-in technique by modulating the amplitude of the external magnetic field at 800 Hz was used to enhance the signal-to-noise ratio (SNR). Temperature-dependent measurements were performed in a closed-cycle cryostat.

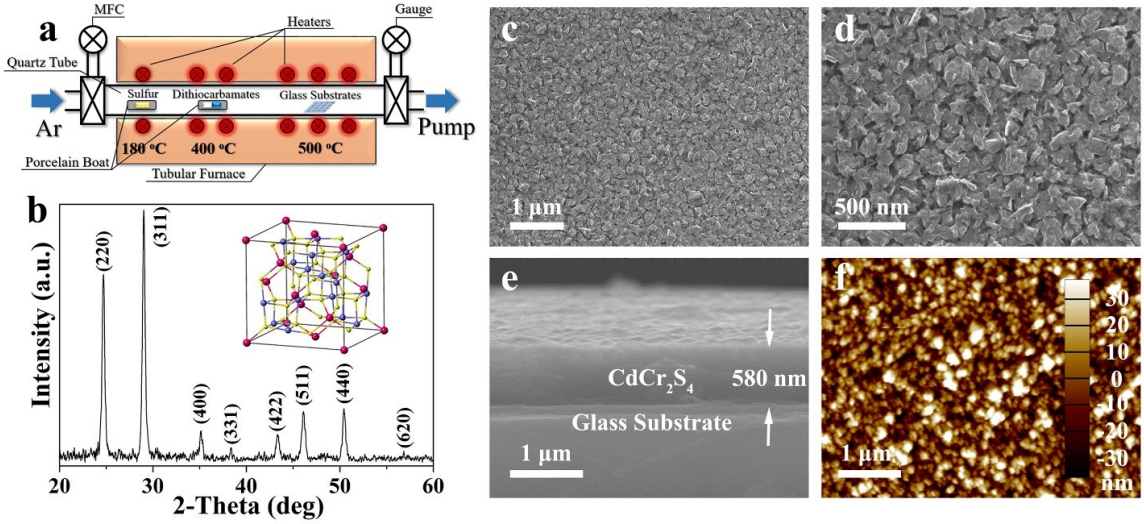

Figure 4.1: Growth of nanostructured $CdCr_2S_4$ film and its crystal structure and morphology characterization. (a) Schematic diagram of the home-built low-pressure MOCVD setup. (b) XRD pattern of polycrystalline $CdCr_2S_4$ film deposited on borosilicate glass substrate. The inset displays the crystal structure of spinel $CdCr_2S_4$ (Cd, pink; Cr, blue; S, yellow). (c) Low- and (d) high-magnification planar SEM images. (e) High-magnification cross-sectional SEM images. (f) 2D AFM image of the $CdCr_2S_4$ film. measurements.

4.4 Results and discussion

Crystal Structure, Crystallinity, and Morphology. Figure 4.1 (a) shows a schematic diagram of the home-built low-pressure MOCVD system. The possible reaction mechanism, crystal structure, and thermogravimetric analysis of $Cd(S_2CNEt_2)_2$ and $Cr(S_2CNEt_2)_3$ are provided in the appendix (figures 4.7 and 4.8). The phase purity and crystallinity of the deposited nanostructured $CdCr_2S_4$ films are confirmed by X-ray diffraction (XRD), as shown in figure 4.1 (b). The films exhibit a face-centered cubic spinel structure with $Fd\bar{3}m$ space group, and the major diffraction peaks are indexed as (220), (311), (400), (331), (422), (511), (440), and (620) planes that match very well with the standard bulk JCPDS $CdCr_2S_4$ pattern no. 16-0506. Based on peak

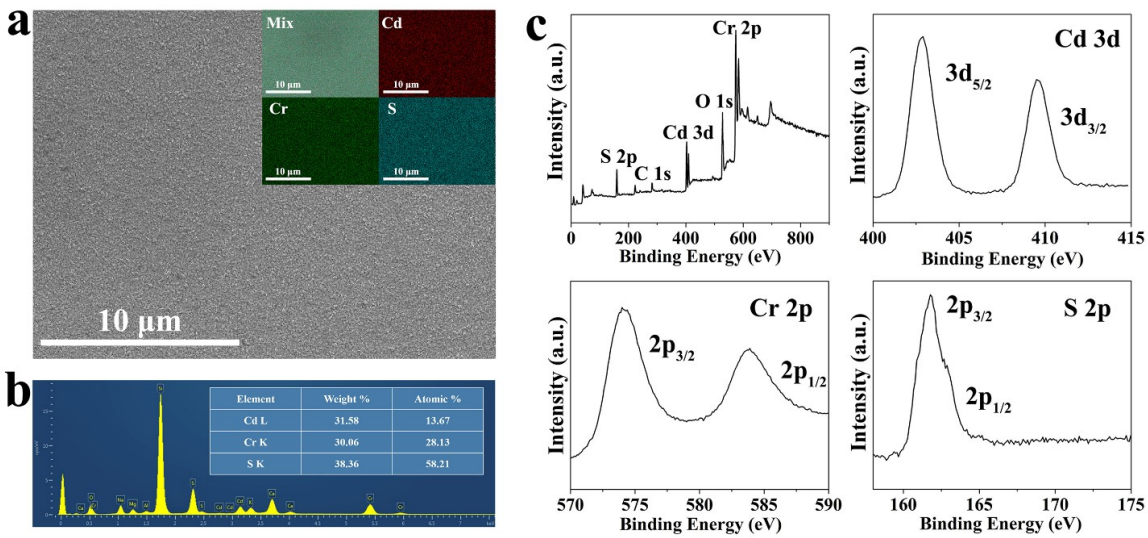

Figure 4.2: Composition and chemical states characterization of the nanostructured $CdCr_2S_4$ film. (a) FESEM image; mixed and individual elemental mapping of the deposited film. (b) EDS spectrum and elemental composition of the film. (c) XPS survey spectrum; high-resolution XPS spectra of Cd 3d, Cr 2p, and S 2p of the $CdCr_2S_4$ film.

positions, the lattice parameter is calculated to be 10.20 Å, which is close to the reported bulk value of 10.24 Å for $CdCr_2S_4$ [25]. In exploring the growth process of $CdCr_2S_4$ films, we find that nonoptimal growth conditions, such as lower deposition temperatures, principally favor formation of wurtzite phase CdS film growth. On the other hand, increasing the deposition temperature results in sulfur deficiency in the deposited films. With changing the amount of precursors or deposition time, the thickness of $CdCr_2S_4$ films can be controlled from $\sim$ 300 to $\sim$ 600 nm with grain sizes from $\sim$ 100 to $\sim$ 200 nm. A 580 nm thick $CdCr_2S_4$ film, which is representative, has been used for structural, optical, and magnetic properties characterization details discussed below.

High-quality nanostructured $CdCr_2S_4$ films are obtained by using the low-pressure MOCVD method under optimal deposition conditions, which have smooth morphology as verified by SEM and AFM, as shown in figures 4.1 (c)-(f). From the low- and high-magnification SEM images in figurers 4.1 (c) and (d), one can clearly observe that the uniform and homogeneous $CdCr_2S_4$ layer fully covers the substrate with a grain size of $\sim$ 150 nm. The $CdCr_2S_4$ layer adheres strongly to borosilicate glass substrates and forms a smooth film surface, which is shiny and reflective.

Unlike most previously reported results showing nonhomogeneous film growth, the MOCVD grown films are dense with uniform grain size and crystallinity over a relatively large area (figure 4.2 (a)). The cross-section SEM image of the nanostructured $CdCr_2S_4$ film (figure 4.1 (e)) further reveals a compact morphology without pinholes. From the two-dimensional (2D) AFM height image in figure 4.1 (f), the root mean square roughness of the film is 18.6 nm for a scan area of 5 $\times$ 5 μm^2.

Chemical Valence and Film Composition. Figure 4.2 (a) presents X-ray energy dispersive spectroscopy (EDS) elemental mapping of the deposited nanostructured $CdCr_2S_4$ film. Based on the EDS result shown in figure 4.2 (b), the Cd/Cr/S ratio is 1:2.05:4.25, which is close to the desired stoichiometry. X-ray photoelectron spectroscopy (XPS) studies have also been performed to investigate the chemical states of the ions in the $CdCr_2S_4$ films. A survey spectrum of the film identified the presence of Cd, Cr, S, O, and C, and high-resolution spectra of Cd 3d, Cr 2p, and S 2p are measured to determine the oxidation states of the constituent elements (figure 4.2 (c)). In the Cd 3d spectrum, peaks at 403.1 and 409.6 eV are ascribed to Cd $3d_{5/2}$ and Cd $3d_{3/2}$, which can be assigned to Cd(II) with peak splitting of 6.5 eV [45]. The Cr 2p spectrum exhibits a spin-orbit separation of 9.6 eV between the Cr $2p_{3/2}$ and Cr $2p_{1/2}$ states, indicative of Cr(III) [46]. The peaks identified at 161.8 and 162.6 eV in the high-resolution spectrum of S are generally attributed to S $2p_{3/2}$ and $2p_{1/2}$, respectively [47]. These results further confirm that the as-deposited films are primarily $CdCr_2S_4$. In brief, the nanostructured $CdCr_2S_4$ films grown by the low-pressure MOCVD method exhibit significantly improved quality than previous chemically synthesized $CdCr_2S_4$ films.

Optical Properties. The optical absorption characteristics of the $CdCr_2S_4$ films are measured by UV-vis spectrophotometry, as shown in figure 4.3 (a). The band gap of $CdCr_2S_4$ is determined to be $\sim$ 2.5 eV for nanoparticles, while thin films and bulk are reported to have a band gap of 2.4-2.6 eV [33, 34, 48].

In figure 4.3 (b), a Tauc plot is obtained from the absorption spectrum of a $CdCr_2S_4$ film (thickness of 580 nm) via the following equation 4.1 [49]:

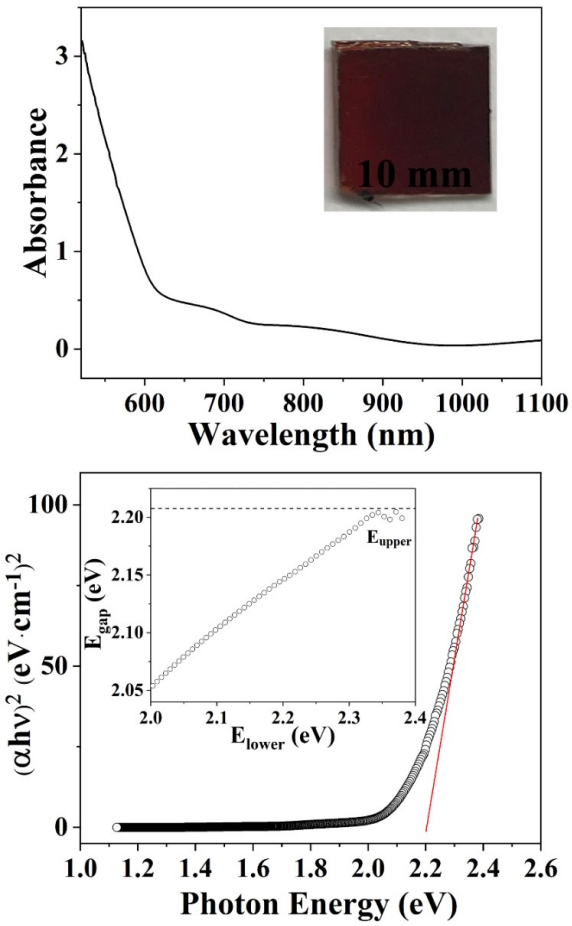

Figure 4.3: Optical properties characterization of the $CdCr_2S_4$ film (thickness of 580 nm). (a) UV-vis absorption spectrum of the $CdCr_2S_4$ film grown on borosilicate glass substrate. The inset shows a photograph of the film. (b) Tauc plot of $(\alpha h\nu)^2$ vs $h\nu$ to determine the band gap of the films. The inset shows the band gap vs lower end of photon energy for fitting.

$$(\alpha h\nu)^n = A(h\nu - E_g) \tag{4.1}$$

where α is the optical absorption coefficient, h is Planck's constant, ν is frequency, E_g is the band gap of the material, A is a constant, and n = 2 or 0.5 for a direct and indirect band gap semiconductor, respectively. Extrapolation of the $(\alpha h\nu)^2$ vs $h\nu$ plot to the photon energy axis gives a direct band gap value of ~ 2.21 eV for our $CdCr_2S_4$ film, where E_{upper} is the highest photon energy in the Tauc plot and E_{lower} is the other end of photon energy for a linear fit.

Magnetic Properties. The static magnetic properties of the $CdCr_2S_4$ films have been mea-

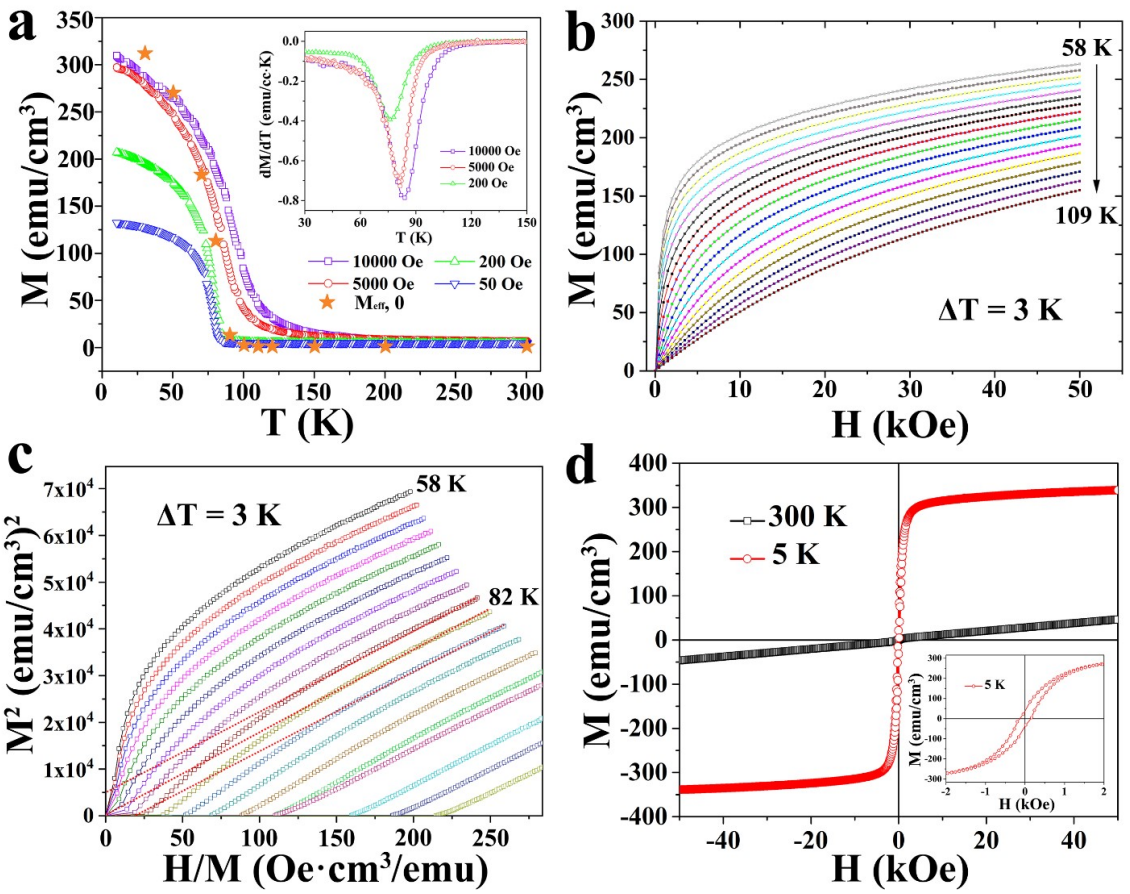

Figure 4.4: Magnetic characterization of the $CdCr_2S_4$ film (thickness of 580 nm). (a) Magnetization (M) versus temperature (T) of the film measured at different magnetic fields. The inset shows plots of the slope, dM/dT, calculated from (a). (b) Representative isothermal M-H measurements and (c) Arrott plots from 58 to 109 K with temperature steps of 3 K. (d) Magnetization as a function of field measured at 5 and 300 K. The inset displays an enlarged portion of the hysteresis loop measured at 5 K.

sured by using a vibrating sample magnetometer (VSM). A series of M-T scans are shown in figure 4.4 (a) for the 580 nm nanostructured film, where the magnetization is plotted as a function of temperature for several different applied magnetic fields. We have also performed isothermal M-H measurements of the magnetization versus applied magnetic field for more accurate determination of the transition temperatures. Representative isothermal plots for the $CdCr_2S_4$ film are given in figure 4.4 (b). On the basis of the isothermal measurements near the transition temperature, we have determined the Curie temperature (T_C) by using the Arrott plot method (isothermal plots of M^2 vs H/M) [50], as shown in figure 4.4 (c). The T_C determined by using this method

is $\sim$ 82 K, which is in good agreement with the reported bulk value of 83 K [25]. Figure 4.4 (d) shows plots of the magnetization as a function of applied magnetic field at 5 and 300 K, respectively. As indicated, the nanostructured $CdCr_2S_4$ film exhibits ferromagnetic behavior at 5 K with a fairly low coercivity value of $\sim$ 170 Oe. The magnetization is $\sim$ 340 emu/cm^3 at a field of 50 kOe, which is close to reported bulk value [51]. As expected, the film is paramagnetic at room temperature, as confirmed by the linear field dependence of the magnetization shown in figure4.4 (d).

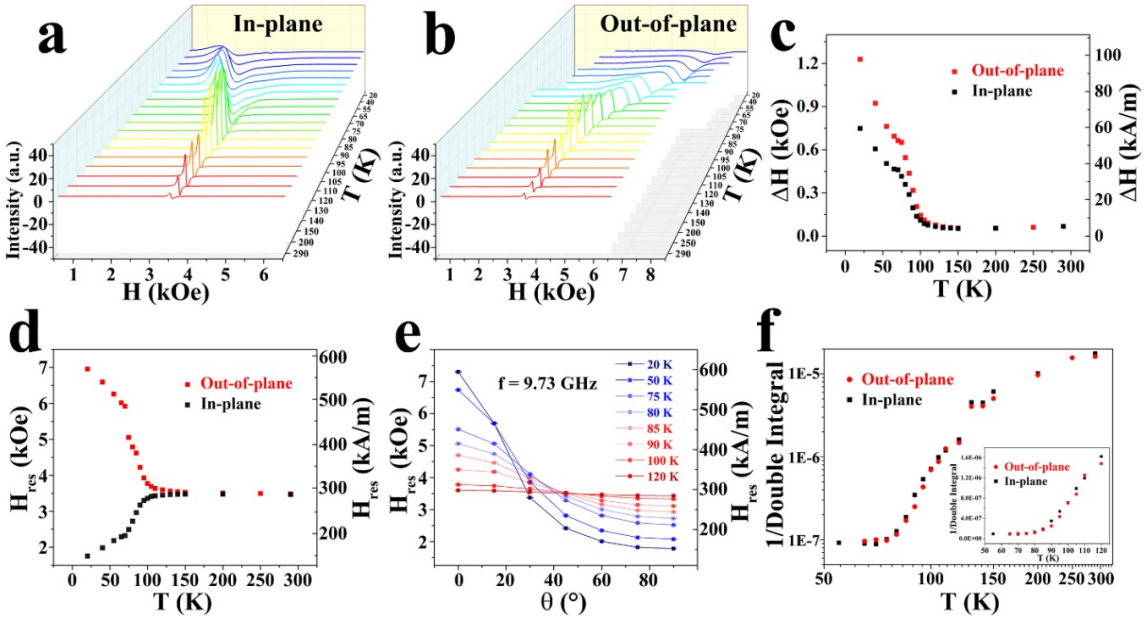

Figure 4.5: CW EPR characterization of the nanostructured $CdCr_2S_4$ film (thickness of 580 nm). (a) EPR spectra as a function of temperature for the film aligned parallel to the external applied magnetic field and (b) perpendicular to the external magnetic field. (c) Line width as a function of temperature for both magnetic field orientations. (d) Resonance field as a function of temperature for both magnetic field orientations. (e) Resonance field as a function of direction of external field (0° perpendicular to film plane and 90° parallel to film plane) at different temperatures. (f) Inverse double integral of CW EPR spectra characterizing the spin susceptibility of the $CdCr_2S_4$ film. The inset displays an enlarged portion around the Curie temperature T_C

Dynamic Magnetic Properties and Magnetic Anisotropy. The dynamic magnetic properties of the $CdCr_2S_4$ films have been investigated by continuous-wave electron paramagnetic resonance (CW EPR, X-band). The EPR spectra are measured in two orientations: one where the film is parallel to the external applied magnetic field (in-plane) and one where it is perpendicular

to the external magnetic field (out-of-plane). The CW EPR signal originates from the localized 3d electrons of Cr^{3+} ions [52, 53]. Figures 4.5 (a) and (b) show the in-plane and out-of-plane CW EPR spectra at temperatures from 20 to 290 K. At high temperatures, the first-derivative EPR peaks for both in-plane and out-of-plane measurements are symmetrical. At the T_C around 80 K the first-derivative EPR peak is the sharpest. As the temperature decreases below T_C, the first-derivative peaks broaden and the peak-to-peak amplitudes decrease, even though the total integrated EPR absorption signal increases. When the magnetic field is in-plane with respect to the film, the peak shifts to lower magnetic field, and when the magnetic field is out-of-plane, the peak shifts to higher magnetic field. The peak-to-peak line widths (ΔH) are plotted in figure 4.5 (c) as a function of temperature for both magnetic field orientations. The EPR spectra of the film are similar regardless of its orientation with respect to the magnetic field in the paramagnetic region, but the linewidth starts to increase below 100 K, indicating the onset of a phase transition. This signifies that the film is magnetized at low temperatures and that the film's internal magnetic field influences its resonance as a function of the external applied field. The temperature dependence of the EPR resonance field (H_{res}) is shown in figure 4.5 (d). The resonance field is constant above the phase transition temperature (paramagnetic region), but below 100 K the Hres decreases when the external field is parallel to the film plane and increases when the external field is perpendicular to the film. This behavior also indicates a phase transition from paramagnetic to ferromagnetic. The difference in H_{res} for in-plane and out-of-plane fields arises from the anisotropy of the film due to dipole-dipole interactions, which renders the film normal as hard axis. To further investigate the magnetic anisotropy for the films, a series of angle- and temperature-dependent EPR spectra have been taken. As shown in figure 4.5 (e), the variation of H_{res} with angle becomes more pronounced as the temperature decreases, indicating a strong anisotropy. The transition from a paramagnetic to ferromagnetic state onset is at $\sim$ 100 K, which is about 17 K above the reported ferromagnetic transition temperature ($\sim$ 83 K)[25]. This indicates that the ferromagnetic phase is stabilized by the presence of a magnetic field, which is also evident in the M vs T plot (figure 4.4 (a)). The temperature dependence of the inverse spin susceptibility, which is pro-

portional to the 1/double integral (DI) of the EPR spectra, is shown in figure 4.5 (f). The inverse of spin susceptibility decreases as temperature drops but ceases to change significantly around T_C and remains constant at lower temperatures.

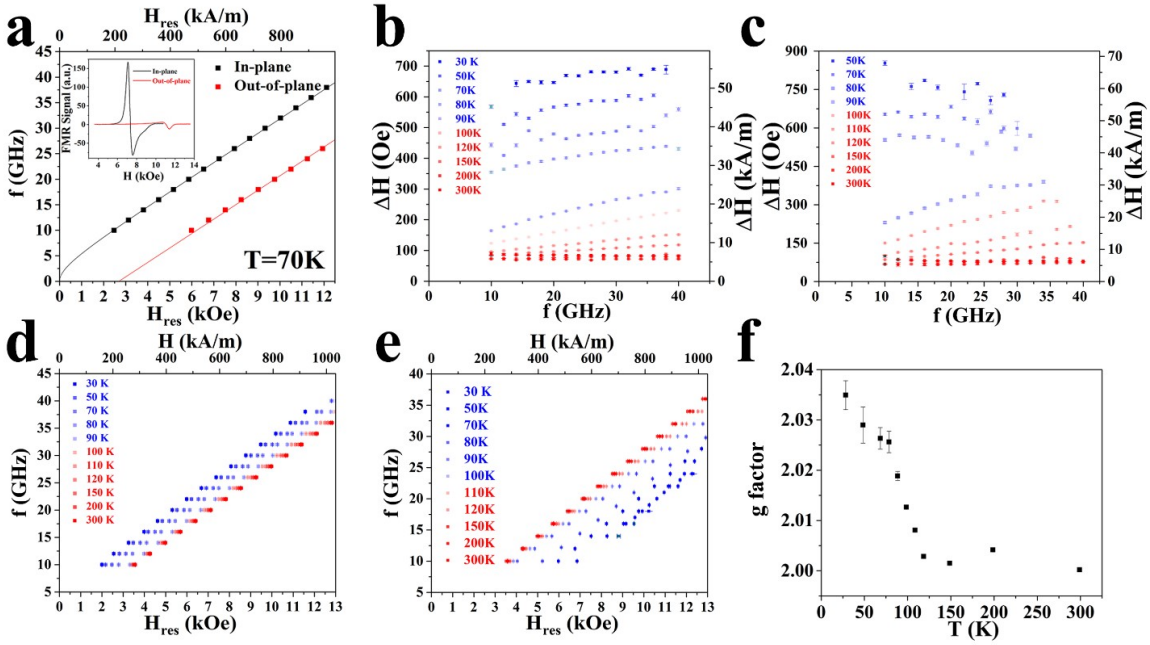

Figure 4.6: Broadband FMR characterization of the $CdCr_2S_4$ film. (a) Representative resonance field as a function of microwave frequency at 70 K for both magnetic field orientations. The continuous line is fit to Kittel's equation. A typical spectrum is shown in the inset. (b) Linewidth as a function of frequency at different temperatures for external magnetic field parallel to film plane and (c) perpendicular to film plane. (d) Kittel plots at different temperatures for external magnetic field parallel to film plane and (e) perpendicular to film. (f) Plot of the extracted g factor as a function of temperature.

T [K]	300	200	150	120	110	100	90	80	70	50	30
γ' [MHz/Oe]	2.799 ± 0.0001	2.805 ± 0.0002	2.801 ± 0.0001	2.803 ± 0.0004	2.811 ± 0.0003	2.817 ± 0.0004	2.825 ± 0.001	2.835 ± 0.003	2.836 ± 0.003	2.839 ± 0.003	2.848 ± 0.005
$M_{eff,0}$ [emu/cm^3]	0 ± 0.1	0 ± 0.4	0 ± 0.7	0 ±2	0± 3	1.4 ± 0.4	82 ± 5	112 ± 3	182 ± 4	269 ± 6	311 ± 2

Table 4.1: Values of effective magnetization $M_{eff,0}$ and gyromagnetic ratio γ' obtained from broadband FMR measurements.

To further investigate the magnetization dynamics and observed anisotropy of the $CdCr_2S_4$ films, broadband ferromagnetic resonance (FMR) measurements have been performed from 10 to 40 GHz at different temperatures, for both in-plane and out-of-plane orientations. By fitting

the FMR spectra to the derivative of a Lorentzian function having both absorptive and dispersive terms, we determine values of the resonance field (H_{res}) and peak-to-peak linewidth (ΔH) [54]. In figure 4.6(a), we show representative H_{res} as a function of FMR frequency (f) at 70 K for both magnetic field orientations. Figures 4.6 (b) and (c) present ΔH as a function of f at different temperatures for both magnetic field orientations, showing a clear increase in ΔH between 80 and 90 K. We fit both in-plane and out-of-plane data to Kittel equations simultaneously with γ' and $M_{eff,0}$ as shared parameters:

$$f_{in-plane} = |\gamma'|\sqrt{H_{res}(H_{res} + 4\pi(M_{eff,0} + \chi H_{res}))} \tag{4.2}$$

$$f_{out-of-plane} = |\gamma'|(H_{res} - 4\pi(M_{eff,0} + \chi H_{res})) \tag{4.3}$$

where $|\gamma'|$ is the absolute value of the gyromagnetic ratio and $M_{eff,0}$ is the effective magnetization extrapolated to zero external field [55]. The above equations are modified Kittel equations, which take into account that the sample magnetization is not constant in the field range used for FMR (cf. figure 4.4 (b)). In a first-order approximation we can assume that the effective magnetization depends linearly on the applied field:

$$M_{eff}(H) = M_{eff,0} + \chi H \tag{4.4}$$

where χ is the magnetic susceptibility. The Kittel plots at different temperatures for both magnetic field orientations are shown in figures 4.6 (d) and (e). The difference between FMR in in-plane and out-of-plane orientations is due to the dipole- dipole interaction and the thin film geometry of the sample, which is also known as shape anisotropy. However, for paramagnetic samples there is no shape anisotropy, which is why there is no difference between the resonance fields for the in-plane and out-of-plane orientation measurements. We have not found evidence of any additional perpendicular anisotropy in the ferromagnetic phase, which may originate for example from interfacial strain. In Table 4.1, we summarize the values of the effective magneti-

zation $M_{eff,0}$ and gyromagnetic ratio $|\gamma'| = \frac{g\mu_B}{h}$ obtained from broadband FMR measurements for the film at different temperatures.

The plot of $M_{eff,0}$ vs T from FMR is plotted together with M vs T from VSM in figure 4.4 (a), showing $M_{eff,0}$ is essentially zero for temperatures above 90 K, and there is sharp increase in $M_{eff,0}$ below 90 K, consistent with the transition temperature determined by using the Arrott plot. The g factor obtained from fitting with the Kittel equations gives a value of ~ 2.00 above 100 K in the paramagnetic region. Below 100 K, the g factor starts to increase as the temperature decreases, further supporting evidence for phase transition to ferromagnetic order. The measured g factors in figure 4.6 (f) are similar to the values reported in bulk and nanocrystal samples [42, 47].

4.5 Conclusion

In summary, we have developed a simple and novel route to grow high-quality spinel $CdCr_2S_4$ nanostructured films via low-pressure metal-organic chemical vapor deposition using synthesized diethyldithiocarbamate complexes as precursors. High-quality ferromagnetic semiconducting $CdCr_2S_4$ films are obtained by the reaction of $Cd(S_2CNEt_2)_2$ and $Cr(S_2CNEt_2)_3$ in the presence of sulfur vapor under relatively mild deposition conditions. Phase-pure $CdCr_2S_4$ films are grown on borosilicate glass substrates, with uniform and homogeneous morphology. The optical properties, static magnetic properties, dynamic magnetic properties, and magnetic anisotropy of the nanostructured $CdCr_2S_4$ films have been systematically investigated. This work offers a novel strategy and a guiding chemical deposition route for the growth of high-quality chalcogenide spinel films. We believe that the MOCVD method using metal dithiocarbamate and other related precursors can be extended to the growth of a variety of other chalcogenide-based magnetic semiconductors for different applications.

4.6 Acknowledgment

This research was supported by the U.S. National Science Foundation under Grant CHE-1508259, the Natural Science Foundation of China (Nos. 51425202, 51772150), the Natural Science Foundation of Jiangsu Province (BK20160093), and the project funded by the Priority Academic Program Development of Jiangsu Higher Education Institutions. As a joint Ph.D. student, C.P. was partially supported by the China Scholarship Council. A.S. would like to acknowledge support through NASA Grant CAN80NSSC18M0023. The authors acknowledge the help received from Dr. Chan-Woong Na during the initial phase of the work.

4.7 Appendix

Reaction mechanism and crystal structure of $Cd(S_2CNEt_2)_2$ and $Cr(S_2CNEt_2)_3$.

The reaction mechanism and crystal structure of the $Cd(S_2CNEt_2)_2$ and $Cr(S_2CNEt_2)_3$ precursors are presented in figure 4.7. In the solid state, the $Cd(S_2CNEt_2)_2$ complex is bi-nuclear, with the two halves of the molecule related by a center of symmetry in order to fill the coordination sphere. For $Cr(S_2CNEt_2)_3$ tris-dithiocarbamate precursor, its octahedral coordination sphere is satisfied by three bidentate dithiocarbamate ligands.

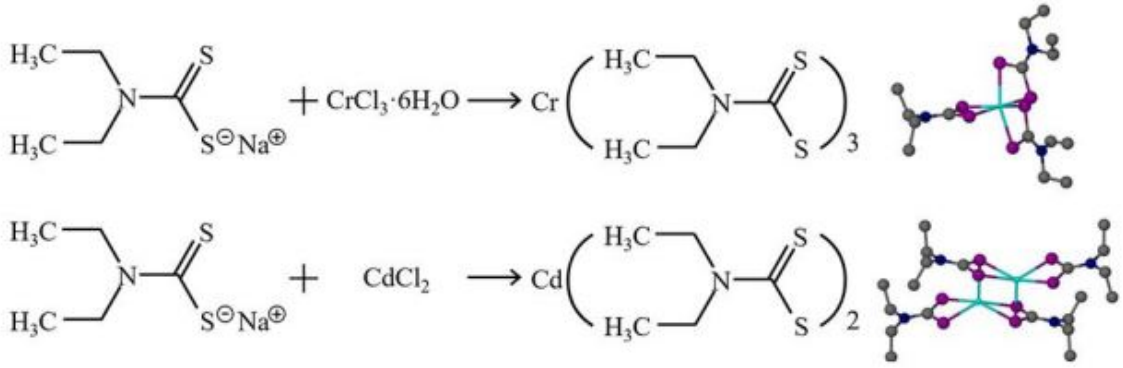

Figure 4.7: The reactions for formation and crystal structure of $Cr(S_2CNEt_2)_3$ and dimerized $Cd(S_2CNEt_2)_2$.

Thermal decomposition of $Cd(S_2CNEt_2)_2$ and $Cr(S_2CNEt_2)_3$.

To study the thermal stability and decomposition temperature, thermogravimetric analysis (TGA) was performed on both the synthesized $Cd(S_2CNEt_2)_2$ and $Cr(S_2CNEt_2)_3$ precursors in a nitrogen atmosphere. As shown in figure 4.8, the thermolysis of $Cd(S_2CNEt_2)_2$ starts at 300 °C and that for $Cr(S_2CNEt_2)_3$ from 350 °C. Based on the TGA weight loss data calculations, the thermolysis products are CdS and Cr_2S_3, respectively.

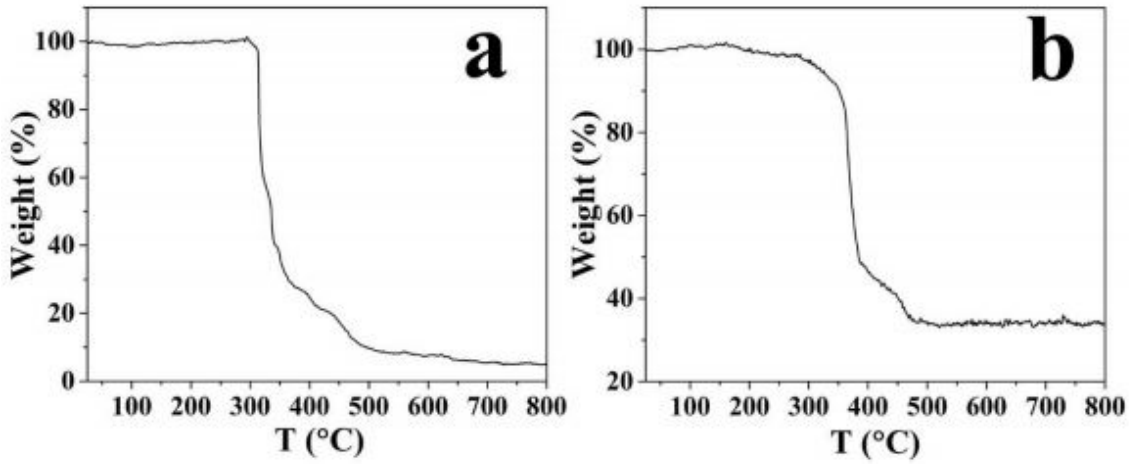

Figure 4.8: Thermogravimetric analysis (TGA) curves for the decomposition of (a) $Cd(S_2CNEt_2)_2$ and (b) $Cr(S_2CNEt_2)_3$.

4.8 References

[1] H. Munekata, H. Ohno, S. Von Molnar, A. Segmüller, L. Chang, and L. Esaki, *Diluted magnetic III-V semiconductors*, Physical Review Letters **63**, 1849 (1989).

[2] C. Mao, D. J. Solis, B. D. Reiss, S. T. Kottmann, R. Y. Sweeney, A. Hayhurst, G. Georgiou, B. Iverson, and A. M. Belcher, *Virus-based toolkit for the directed synthesis of magnetic and semiconducting nanowires*, Science **303**, 213 (2004).

[3] M. D. Regulacio, K. Bussmann, B. Lewis, and S. L. Stoll, *Magnetic properties of lanthanide chalcogenide semiconducting nanoparticles*, Journal of the American Chemical Society **128**, 11173 (2006).

[4] M. A. Rahman, S. Rout, J. P. Thomas, D. McGillivray, and K. T. Leung, *Defect-rich dopant-free ZrO_2 nanostructures with superior dilute ferromagnetic semiconductor properties*, Journal of the American Chemical Society **138**, 11896 (2016).

[5] C. Huang, J. Feng, F. Wu, D. Ahmed, B. Huang, H. Xiang, K. Deng, and E. Kan, *Toward intrinsic room-temperature ferromagnetism in two-dimensional semiconductors*, Journal of the American Chemical Society **140**, 11519 (2018).

[6] S. Wolf, D. Awschalom, R. Buhrman, J. Daughton, v. S. von Molnár, M. Roukes, A. Y. Chtchelkanova, and D. Treger, *Spintronics: a spin-based electronics vision for the future*, Science **294**, 1488 (2001).

[7] Z.-P. Lv, Z.-Z. Luan, H.-Y. Wang, S. Liu, C.-H. Li, D. Wu, J.-L. Zuo, and S. Sun, *Tuning electron-conduction and spin transport in magnetic iron oxide nanoparticle assemblies via tetrathiafulvalene-fused ligands*, ACS Nano **9**, 12205 (2015).

[8] R. Seshadri, *Zinc oxide-based diluted magnetic semiconductors*, Current Opinion in Solid State and Materials Science **9**, 1 (2005).

[9] Y. Hou and D. J. Sellmyer, *Magnetic nanomaterials: Fundamentals, synthesis and applications* (John Wiley & Sons, 2017).

[10] T. Dietl, *A ten-year perspective on dilute magnetic semiconductors and oxides*, Nature Materials **9**, 965 (2010).

[11] T. Dietl and H. Ohno, *Dilute ferromagnetic semiconductors: Physics and spintronic structures*, Reviews of Modern Physics **86**, 187 (2014).

[12] N. Ray, V. Gupta, L. Sarma, P. Kush, J. Nag, and S. Sapra, *Tuning the electronic and magnetic properties of $CuAlO_2$ nanocrystals using magnetic dopants*, ACS Omega **3**, 509 (2018).

[13] D. D. Awschalom and M. E. Flatté, *Challenges for semiconductor spintronics*, Nature Physics **3**, 153 (2007).

[14] W. Prellier, A. Fouchet, and B. Mercey, *Oxide-diluted magnetic semiconductors: a review of the experimental status*, Journal of Physics: Condensed Matter **15**, R1583 (2003).

[15] D. B. Mitzi, *Solution-processed inorganic semiconductors*, Journal of Materials Chemistry **14**, 2355 (2004).

[16] P. Baltzer, P. Wojtowicz, M. Robbins, and E. Lopatin, *Exchange interactions in ferromagnetic chromium chalcogenide spinels*, Physical Review **151**, 367 (1966).

[17] F. Lotgering, *Ferromagnetism in spinels: $CuCr_2S_4$ and $CuCr_2Se_4$*, Solid State Communications **2**, 55 (1964).

[18] P. Baltzer, H. Lehmann, and M. Robbins, *Insulating ferromagnetic spinels*, Physical Review Letters **15**, 493 (1965).

[19] Y.-H. A. Wang, A. Gupta, M. Chshiev, and W. H. Butler, *Half-metallic electronic structures of quaternary ferromagnetic chalcospinels: $Cd_xCu_{(1-x)}Cr_2S_4$ and $Cd_xCu_{(1-x)}Cr_2Se_4$*, Applied Physics Letters **92**, 062507 (2008).

[20] Y.-H. Wang, A. Gupta, M. Chshiev, and W. Butler, *Induced half-metallicity in Cr-based ferromagnetic chalcospinels with anion substitutions: $CuCr_2SSe_{(4-x)}E_x$ (E= F, Cl, Br), $CuCdCr_2SSe_{(4-x)}$, and $CdCr_2SSe_{(4-x)}D_x$ (D= N, P, As)*, Applied Physics Letters **94**, 062515 (2009).

[21] W. L. Lee, S. Watauchi, V. Miller, R. J. Cava, and N. P. Ong, *Dissipationless anomalous Hall current in the ferromagnetic spinel $CuCr_2Se_{(4-x)}Br_x$*, Science **303**, 1647 (2004).

[22] R. Wiesendanger, *Nanoscale magnetic skyrmions in metallic films and multilayers: a new twist for spintronics*, Nature Reviews Materials **1**, 16044 (2016).

[23] H. Göbel, *Local lattice distortions in chromium chalcogenide spinels at low temperatures*, Journal of Magnetism and Magnetic Materials **3**, 143 (1976).

[24] G. Harbeke and H. Pinch, *Magnetoabsorption in single-crystal semiconducting ferromagnetic spinels*, Physical Review Letters **17**, 1090 (1966).

[25] J. Hemberger, P. Lunkenheimer, R. Fichtl, H.-A. K. Von Nidda, V. Tsurkan, and A. Loidl, *Relaxor ferroelectricity and colossal magnetocapacitive coupling in ferromagnetic $CdCr_2S_4$*, Nature **434**, 364 (2005).

[26] C. Sun, C. Huang, C. Lin, J. Her, C. Ho, J.-Y. Lin, H. Berger, and H. Yang, *Colossal electroresistance and colossal magnetoresistance in spinel multiferroic $CdCr_2S_4$*, Applied Physics Letters **96**, 122109 (2010).

[27] V. Tsurkan, D. Ehlers, V. Felea, H.-A. K. von Nidda, and A. Loidl, *Critical magnetic behavior of ferromagnetic $CdCr_2S_4$*, Physical Review B **88**, 144417 (2013).

[28] G. Harbeke and H. Lehmann, *Optical transitions and band structure model for cadmium chromium chalcogenides*, Solid State Communications **8**, 1281 (1970).

[29] Y.-H. A. Wang, N. Bao, L. Shen, P. Padhan, and A. Gupta, *Size-controlled synthesis of magnetic CuCr2Se4 nanocrystals*, Journal of the American Chemical Society **129**, 12408 (2007).

[30] K. Ramasamy, D. Mazumdar, Z. Zhou, Y.-H. A. Wang, and A. Gupta, *Colloidal synthesis of magnetic $CuCr_2S_4$ nanocrystals and nanoclusters*, Journal of the American Chemical Society **133**, 20716 (2011).

[31] K. Ramasamy, D. Mazumdar, R. D. Bennett, and A. Gupta, *Syntheses and magnetic properties of Cr_2Te_3 and $CuCr_2Te_4$ nanocrystals*, Chemical Communications **48**, 5656 (2012).

[32] K. Ramasamy, H. Sims, S. Keshavarz, N. Naghibolashrafi, and A. Gupta, *Nanocrystals of $CuCr_2S_{(4-x)}Se_x$ chalcospinels with tunable magnetic properties*, Journal of Materials Chemistry C **4**, 3628 (2016).

[33] C. Pang, L. Gao, A. V. Singh, H. Chen, M. K. Bowman, N. Bao, L. Shen, and A. Gupta, *Synthesis, formation mechanism, and magnetic properties of monodisperse semiconducting spinel $CdCr_2S_4$ nanocrystals via a facile "seed-mediated" growth method*, Chemistry of Materials **30**, 1701 (2018).

[34] S. Lade, M. Uplane, M. Uplane, and C. Lokhande, *Electrosynthesis of $CdCr_2S_4$ thin films and their characterization*, Materials Chemistry and Physics **53**, 185 (1998).

[35] R. Mane, B. Sankapal, K. Gadave, and C. Lokhande, *Preparation of $CdCr_2S_4$ and $HgdCr_2S_4$ thin films by chemical bath deposition*, Materials Research Bulletin **34**, 2035 (1999).

[36] A. Salem and M. El-Ghazzawi, *Structural and optical properties of chemically deposited CdCr2S4 thin films*, Semiconductor Science and Technology **19**, 236 (2003).

[37] T. Mahalingam, S. Thanikaikarasan, V. Dhanasekaran, R. Mariappan, P. Jayamurugan, S. Velumani, and J.-K. Rhee, *Electrochemical deposition and studies on $CdCr_2S_4$ thin films*, Materials Science and Engineering: B **174**, 249 (2010).

[38] Y. Xie, Z. Yang, L. Li, L. Yin, X. Hu, Y. Huang, H. Jian, W. Song, Y. Sun, S. Zhou, *et al.*, *Annealing induced colossal magnetocapacitance and colossal magnetoresistance in In-doped $CdCr_2S_4$*, Journal of Applied Physics **112**, 123912 (2012).

[39] O. Hartmann, G. M. Kalvius, R. Wäppling, A. Günther, V. Tsurkan, A. Krimmel, and A. Loidl, *Magnetic properties of the multiferroic chromium thio-spinels $CdCr_2S_4$ and $HgCr_2S_4$*, The European Physical Journal B **86**, 148 (2013).

[40] S. Krohns, F. Schrettle, P. Lunkenheimer, V. Tsurkan, and A. Loidl, *Colossal magnetocapacitive effect in differently synthesized and doped $CdCr_2S_4$*, Physica B: Condensed Matter **403**, 4224 (2008).

[41] S. Faÿ, J. Steinhauser, S. Nicolay, and C. Ballif, *Polycrystalline ZnO: B grown by LPCVD as TCO for thin film silicon solar cells*, Thin Solid Films **518**, 2961 (2010).

[42] K. Jensen and D. Graves, *Modeling and analysis of low pressure CVD reactors*, Journal of the Electrochemical Society **130**, 1950 (1983).

[43] D. J. Lewis, A. A. Tedstone, X. L. Zhong, E. A. Lewis, A. Rooney, N. Savjani, J. R. Brent, S. J. Haigh, M. G. Burke, C. A. Muryn, *et al.*, *Thin films of molybdenum disulfide doped with chromium by aerosol-assisted chemical vapor deposition (AACVD)*, Chemistry of Materials **27**, 1367 (2015).

[44] A. A. Memon, M. Afzaal, M. A. Malik, C. Q. Nguyen, P. O'Brien, and J. Raftery, *The N-alkyldithiocarbamato complexes [M(S2CNHR)2] (M = Cd(ii) Zn(ii); R = C2H5, C4H9, C6H13, C12H25); their synthesis, thermal decomposition and use to prepare of nanoparticles and nanorods of CdS*, Dalton Trans. , 4499 (2006).

[45] T. Nakanishi, B. Ohtani, and K. Uosaki, *Fabrication and characterization of CdS-nanoparticle mono-and multilayers on a self-assembled monolayer of alkanedithiols on gold*, The Journal of Physical Chemistry B **102**, 1571 (1998).

[46] E. Malicka, A. Waśkowska, J. Heimann, R. Sitko, and D. Kaczorowski, *Structural and magnetic properties of $CuCr_2Se_4$ single crystals diluted with Sb (III)*, Journal of Alloys and Compounds **513**, 353 (2012).

[47] A. Singh, H. Geaney, F. Laffir, and K. M. Ryan, *Colloidal synthesis of wurtzite Cu_2ZnSnS_4 nanorods and their perpendicular assembly*, Journal of the American Chemical Society **134**, 2910 (2012).

[48] S. Berger and L. Ekstrom, *Optical Properties of Single-Crystal Films of $CdCr_2S_4$*, Physical Review Letters **23**, 1499 (1969).

[49] J. Tauc, *Optical properties and electronic structure of amorphous Ge and Si*, Materials Research Bulletin **3**, 37 (1968).

[50] A. Arrott, *Criterion for ferromagnetism from observations of magnetic isotherms*, Physical Review **108**, 1394 (1957).

[51] L. Yan, J. Shen, Y. Li, F. Wang, Z. Jiang, F. Hu, J. Sun, and B. Shen, *Large magnetocaloric effect in spinel $CdCr_2S_4$*, Applied physics letters **90**, 262502 (2007).

[52] L. Zhang, L. Li, R. Li, J. Fan, L. Ling, W. Tong, Z. Qu, S. Tan, and Y. Zhang, *Spin-lattice coupling studied by magnetic entropy and EPR in the $CdCr_2S_4$ system*, Solid State Communications **150**, 2109 (2010).

[53] L. Zhang, W. Tong, J. Fan, C. Zhang, R. Li, and Y. Zhang, *ESR study of the ferrimagnetic spinel selenide $CuCr_2Se_4$*, The European Physical Journal B **83**, 325 (2011).

[54] C. Oates, F. Ogrin, P. Riedi, S. Lee, G. Smith, and T. Thomson, *High field ferromagnetic resonance and torque magnetometry of longitudinal recording media*, Journal of Magnetism and Magnetic Materials **242**, 402 (2002).

[55] B. Khodadadi, J. B. Mohammadi, C. Mewes, T. Mewes, M. Manno, C. Leighton, and C. W. Miller, *Enhanced spin pumping near a magnetic ordering transition*, Physical Review B **96**, 054436 (2017).

CHAPTER 5

CONCLUSION

To conclude this dissertation, it is shown that the broadband FMR technique is a very powerful tool to investigate various magnetic properties of magnetic materials. Even some properties which are not easy to investigate by other means can be investigated indirectly by broadband FMR. For example, evidence of a structural phase transition in magnetite thin films was investigated in this dissertation.

The FMR investigation of as-cast ribbon of nanocomposite $Co_{74.6}Fe_{2.7}Mn_{2.7}Nb_4Si_2B_{14}$ soft magnetic alloy, which is amorphous in structure showed that it is magnetically isotropic. But annealing the ribbon under stress induces an in-plane uniaxial anisotropy. The magnitude of anisotropy increases with the stress applied during annealing. The in-plane uniaxial anisotropy determined from the broadband FMR data and the permeability calculated from it is in good agreement with the values determined using vibrating sample magnetometry and impedance spectrometry of toroidal cores. Due to its non-destructive nature and relative ease of use, this new method of determining permeability from broadband FMR technique, could be used as an in-line method for determining the permeability in industry scale systems for quality control. In addition to offering a new way to determine the permeability of samples, FMR at the same time also enables the precise measurement of the effective magnetization and the effective damping parameter. As a future project, the FMR study of amorphous ribbons annealed at different temperatures will be an interesting system to investigate. The crystallization of the amorphous ribbons due to annealing affects their magnetic properties and it will be interesting to investigate these properties. This may give some insights into the correlation between the magnetization dynamics and the constituent structure of the ribbon. The study of thin films of these nanocomposite alloys are

also important for future device applications.

In the investigation of a magnetite thin film of thickness 30 nm grown on $MgGa_2O_4(001)$ substrate by broadband FMR, the Verwey transition temperature was found to be $\sim$ 110 K which is same as the transition temperature as obtained by resistance vs temperature measurement, but significantly lower than the bulk value $\sim$ 120 K, despite having improved structural quality. This suggests that the substrate induced strain in the film strongly affects the Verwey transition temperature. The magnetocrystalline anisotropy is also affected by strain. Another interesting observation is that the in-plane uniaxial anisotropy below the Verwey transition evolves gradually as the temperature decreases, suggesting that the cubic-monoclinic phase transition occurs continuously over a wide temperature range. The isotropic point, i.e. the temperature at which magnetocrystalline anisotropy vanishes, is found to be approximately 120 K, which is 10 K lower than the bulk value. The resonance linewidth and effective damping increases abruptly below 110 K. The effective damping constant is determined to be $\sim$ 0.01 and is independent of temperature from 300 K to 120 K. However, below 120 K, the damping and the magnetic inhomogeneity increase sharply. The study of the magnetization dynamics through the Verwey transition presented in this thesis could be extended to magnetite films grown on different isostructural substrates to investigate the influence of the lattice mismatch. Such a study can reveal more information about how the strain affects the Verwey transition. Broadband FMR studies of bulk magnetite single crystals will be helpful to compare the effects of the substrate on the properties of thin magnetite films in contrast with bulk crystals.

Lastly, in the study of nanostructured $CdCr_2S_4$ films grown by low-pressure MOCVD on a glass substrate, the para-ferro phase transition is found to be at $T_c \sim 81$ K. This broadband FMR result was confirmed by Arrot plot method (plots of M^2 vs H/M) of independant VSM data. This value of T_c is in good agreement with the reported bulk value of 83 K. The FMR in this study is measured in two configurations of external magnetic fields: one where magnetic field is parallel to the film plane (in-plane) and one where it is perpendicular to the film plane (out-of-plane). The effective magnetization obtained from FMR extrapolated to zero field gives better approxi-

mation of the saturation magnetization as a function of temperature than the magnetization obtained from VSM data. The in-plane and out-of-plane FMR measurements show no difference in resonance field (H_{res}) position in the paramagnetic phase (above T_c) clearly indicating that the demagnetizing field is negligibly small, as it should be. As the temperature is decreased below T_c, the in-plane and out-of-plane resonance positions start to differ, the out-of-plane resonance position starts increasing indicating that a significant demagnetizing field develops as a result of transitioning to the ferromagnetic phase. The g factor extracted from FMR is ~ 2.00 for the paramagnetic phase, suggesting a spin only (no orbital contribution) origin of the magnetic moment. As the film goes into ferromagnetic phase the g factor starts increasing indicating small orbital contribution. The present study of $CdCr_2S_4$ was done using a polycrystalline film, which does not provide information about the role of the magnetocrystalline anisotropy. A similar broadband FMR study of a single crystal thin film would be interesting to carry out in the future because it will provide a detailed information about the evolution of the magnetocrystalline anisotropy as the paramagnetic to ferromagnetic phase transition occurs.

REFERENCES

[1] A. Stupakiewicz, A. Maziewski, I. Davidenko, and V. Zablotskii, *Light-induced magnetic anisotropy in Co-doped garnet films*, Physical Review B **64**, 064405 (2001).

[2] B. Sharp and R. Teale, *Photo-induced changes in the magnetic anisotropy of silicon-doped yttrium iron garnet*, Journal of Physics C: Solid State Physics **7**, 965 (1974).

[3] T. L. Gilbert, *A phenomenological theory of damping in ferromagnetic materials*, IEEE Transactions on Magnetics **40**, 3443 (2004).

[4] L. Landau and Lifshitz, *On the theory of the dispersion of magnetic permeability in ferromagnetic bodies*, Phys. Z. Sowjetunion. **8**, 153 (1935).

[5] C. Kittel, *On the theory of ferromagnetic resonance absorption*, Physical Review **73**, 155 (1948).

[6] A. G. Gurevich and G. A. Melkov, *Magnetization oscillations and waves* (CRC press, 1996).

[7] W. H. Meiklejohn and C. P. Bean, *New magnetic anisotropy*, Physical Review **102**, 1413 (1956).

[8] J. Nogués and I. K. Schuller, *Exchange bias*, Journal of Magnetism and Magnetic Materials **192**, 203 (1999).

[9] J. Smith and H. Beljers, *Ferromagnetic resonance absorbtion in $BaFe_{12}O_{19}$, a highly anisotropic crystal*, Philips Res. Rep **10**, 113 (1955).

[10] M. Hurben and C. Patton, *Theory of two magnon scattering microwave relaxation and ferromagnetic resonance linewidth in magnetic thin films*, Journal of Applied Physics **83**, 4344 (1998).

[11] V. Flovik, F. Macià, A. D. Kent, and E. Wahlström, *Eddy current interactions in a ferromagnet-normal metal bilayer structure, and its impact on ferromagnetic resonance lineshapes*, Journal of Applied Physics **117**, 143902 (2015).

[12] J. Lock, *Eddy current damping in thin metallic ferromagnetic films*, British Journal of Applied Physics **17**, 1645 (1966).

[13] S. Takahashi, *Physical principles of spin pumping*, in *Handbook of Spintronics*, edited by Y. Xu, D. D. Awschalom, and J. Nitta (Springer Netherlands, Dordrecht, 2016) pp. 1445–1480.

[14] C. K. Mewes and T. Mewes, *Relaxation in magnetic materials for spintronics*, Handbook of Nanomagnetism , 71 (2015).

[15] J. H. Griffiths, *Anomalous high-frequency resistance of ferromagnetic metals*, Nature **158**, 670 (1946).

[16] C. Kittel, *Interpretation of anomalous Larmor frequencies in ferromagnetic resonance experiment*, Physical Review **71**, 270 (1947).

[17] C. Oates, F. Ogrin, S. Lee, P. Riedi, G. Smith, and T. Thomson, *High field ferromagnetic resonance measurements of the anisotropy field of longitudinal recording thin-film media*, Journal of Applied Physics **91**, 1417 (2002).

[18] H. M. Swartz, *Electron Spin Resonance: A comprehensive treatise on experimental techniques by CP Poole, Jr.*, Medical Physics **11**, 568 (1984).

[19] J. H. Scofield, *Frequency-domain description of a lock-in amplifier*, American Journal of Physics **62**, 129 (1994).

[20] W. C. Michels and N. L. Curtis, *A pentode lock-in amplifier of high frequency selectivity*, Review of Scientific Instruments **12**, 444 (1941).

[21] E. Chen, D. Apalkov, Z. Diao, A. Driskill-Smith, D. Druist, D. Lottis, V. Nikitin, X. Tang, S. Watts, S. Wang, *et al.*, *Advances and future prospects of spin-transfer torque random access memory*, IEEE Transactions on Magnetics **46**, 1873 (2010).

[22] B. Tudu and A. Tiwari, *Recent developments in perpendicular magnetic anisotropy thin films for data storage applications*, Vacuum **146**, 329 (2017).

[23] N. Aronhime, V. DeGeorge, V. Keylin, P. Ohodnicki, and M. E. McHenry, *The effects of strain-annealing on tuning permeability and lowering losses in Fe-Ni-based metal amorphous nanocomposites*, JOM **69**, 2164 (2017).

[24] A. Srivastava, K. Cole, A. Wadsworth, T. Burton, C. Mewes, T. Mewes, G. B. Thompson, R. D. Noebe, and A. M. Leary, *Broadband characterization of stress induced anisotropy in nanocomposite* $Co_{74.6}Fe_{2.7}Mn_{2.7}Nb_4Si_2B_{14}$, Journal of Magnetism and Magnetic Materials **500**, 166307 (2020).

[25] A. V. Singh, A. Srivastava, J. B. Mohammadi, S. Regmi, U. Bhat, R. Datta, T. Mewes, and A. Gupta, *Studies of electrical and magnetic properties across the Verwey transition in epitaxial magnetite thin films*, Journal of Applied Physics **126**, 093902 (2019).

[26] F. Walz, *The Verwey transition-a topical review*, Journal of Physics: Condensed Matter **14**, R285 (2002).

[27] C. Pang, A. Srivastava, M. M. Lockart, T. Mewes, M. K. Bowman, N. Bao, L. Shen, and A. Gupta, *Magnetic properties of semiconducting spinel* $CdCr_2S_4$ *nanostructured films grown by low-pressure metal-organic chemical vapor deposition*, ACS Applied Electronic Materials **1**, 1424 (2019).

[28] B. Khodadadi, A. Rai, A. Sapkota, A. Srivastava, B. Nepal, Y. Lim, D. A. Smith, C. Mewes, S. Budhathoki, A. J. Hauser, *et al.*, *Conductivitylike Gilbert damping due to intraband scattering in epitaxial Iron*, Physical Review Letters **124**, 157201 (2020).

[29] Z. Li, J. Krieft, A. V. Singh, S. Regmi, A. Rastogi, A. Srivastava, Z. Galazka, T. Mewes, A. Gupta, and T. Kuschel, *Vectorial observation of the spin Seebeck effect in epitaxial $NiFe_2O_4$ thin films with various magnetic anisotropy contributions*, Applied Physics Letters **114**, 232404 (2019).

[30] B. Khodadadi, J. B. Mohammadi, J. M. Jones, A. Srivastava, C. Mewes, T. Mewes, and C. Kaiser, *Interlayer exchange coupling in asymmetric Co- Fe/Ru/Co- Fe trilayers investigated with broadband temperature-dependent ferromagnetic resonance*, Physical Review Applied **8**, 014024 (2017).

[31] E. Verwey, *Electronic conduction of magnetite (Fe_3O_4) and its transition point at low temperatures*, Nature **144**, 327 (1939).